

1 **Calibrating the temporal and spatial dynamics of the Ediacaran - Cambrian**  
2 **radiation of animals**

3  
4 Fred T. Bowyer<sup>1,2\*</sup>, Andrey Yu. Zhuravlev<sup>3</sup>, Rachel Wood<sup>2</sup>, Graham A. Shields<sup>4</sup>, Ying Zhou<sup>4</sup>,  
5 Andrew Curtis<sup>2</sup>, Simon W. Poulton<sup>1</sup>, Daniel J. Condon<sup>5</sup>, Chuan Yang<sup>5</sup> and Maoyan Zhu<sup>6,7</sup>

6  
7 <sup>1</sup>School of Earth and Environment, University of Leeds, Leeds LS2 9JT, UK.

8 <sup>2</sup>School of GeoSciences, University of Edinburgh, James Hutton Road, Edinburgh EH9 3FE, UK.

9 <sup>3</sup>Department of Biological Evolution, Faculty of Biology, Lomonosov Moscow State University Leninskie Gory  
10 1(12), Moscow 119234, Russia.

11 <sup>4</sup>Department of Earth Sciences, University College London, Gower Street, London WC1E 6BT, UK.

12 <sup>5</sup>British Geological Survey, Keyworth, NG12 5GG, UK

13 <sup>6</sup>State Key Laboratory of Palaeobiology and Stratigraphy, Nanjing Institute of Geology and Palaeontology and  
14 Center for Excellence in Life and Palaeoenvironment, Chinese Academy of Sciences, Nanjing 210008, China.

15 <sup>7</sup>College of Earth and Planetary Sciences, University of Chinese Academy of Sciences, Beijing 10049, China.

16  
17  

---

18 This is a preprint submitted to EarthArXiv. This manuscript has been peer-reviewed and formally  
19 accepted for publication in Earth-Science Reviews. Once the manuscript is in press, it will be  
20 available via the 'Peer-reviewed Publication DOI' link on the right-hand side of this webpage.  
21 Please feel free to contact any of the authors; we welcome feedback.

22  

---

23 \*Please address correspondence to:

24 Email: [fred.bowyer@ed.ac.uk](mailto:fred.bowyer@ed.ac.uk) (Fred T. Bowyer)

25  
26 *Manuscript accepted in Earth-Science Reviews*

*December 23, 2021*

## 27 **Abstract**

28       The Ediacaran-Cambrian transition, which incorporates the radiation of animals, lacks a robust  
29 global temporal and spatial framework, resulting in major uncertainty in the evolutionary dynamics  
30 of this critical radiation and its relationship to changes in palaeoenvironmental geochemistry. We  
31 first present a new  $\delta^{13}\text{C}_{\text{carb}}$  composite reference curve for the Ediacaran Nama Group of southern  
32 Namibia, and we then outline four new possible global age models (A to D) for the interval 551-  
33 517 million years ago (Ma). These models comprise composite carbonate-carbon isotope ( $\delta^{13}\text{C}_{\text{carb}}$ )  
34 curves, which are anchored to radiometric ages and consistent with strontium isotope  
35 chemostratigraphy, and are used to calibrate metazoan distribution in space and time. These  
36 models differ most prominently in the temporal position of the basal Cambrian negative  
37  $\delta^{13}\text{C}_{\text{carb}}$  excursion (BACE). Regions that host the most complete records show that the BACE nadir  
38 always predates the Ediacaran-Cambrian boundary as defined by the first appearance datum (FAD)  
39 of the ichnospecies *Treptichnus pedum*. Whilst treptichnid traces are present in the late Ediacaran  
40 fossil record, the FAD of the ichnospecies *T. pedum* appears to post-date the LAD of in situ  
41 *Cloudina* and *Namacalathus* in all environments with high-resolution  $\delta^{13}\text{C}_{\text{carb}}$  data. Two age  
42 models (A and B) place the BACE within the Ediacaran, and yield an age of ~538.8 Ma for the  
43 Ediacaran-Cambrian boundary; however models C and D appear to be the most parsimonious and  
44 may support a recalibration of the boundary age by up to 3 Myr younger. All age models reveal a  
45 previously underappreciated degree of variability in the terminal Ediacaran, incorporating notable  
46 positive and negative excursions that precede the BACE. Notwithstanding remaining  
47 uncertainties in chemostratigraphic correlation, all models support a pre-BACE first appearance  
48 of Cambrian-type shelly fossils in Siberia and possibly South China, and show that the Ediacaran-  
49 Cambrian transition was a protracted interval represented by a series of successive radiations.

50 **The Ediacaran-Cambrian radiation occurred over a protracted interval without global**  
51 **mass extinctions and with generally diachronous metazoan appearances.**

52

## 53 **1. Introduction**

54 The late Ediacaran to early Cambrian interval encompasses the Gaskiers glaciation (~580 Ma),  
55 the first appearance of complex macroscopic life (~575 Ma), mobile biota ( $\leq 560$  Ma), skeletal  
56 metazoans (~550 Ma), and the origin of modern metazoan phyla (Wood et al., 2019).  
57 Understanding the temporal and spatial context of these events is currently limited due to the lack  
58 of high-resolution age models to allow correlation of key sections. The geological record  
59 throughout this interval also contains numerous unconformities and gaps of uncertain duration, a  
60 sparse global distribution of datable stratiform volcanic deposits, and diverse endemic biotas,  
61 resulting in loose chronostratigraphic and biostratigraphic control. As a result, no consistent global  
62 chronostratigraphic correlation exists, particularly for the critical late Ediacaran to lower Cambrian  
63 (Fortunian Stage) interval. Early metazoans evolved in a highly dynamic Earth system, and so  
64 without a high-resolution temporal and spatial framework we are unable to address many profound  
65 uncertainties, including the evolutionary dynamics of the Cambrian Explosion, the response of  
66 metazoans to local and global changes in oceanic redox conditions and nutrient availability, and  
67 whether one or more contemporaneous mass extinctions occurred.

68 The formal placement of the Ediacaran-Cambrian boundary in the Fortune Head section,  
69 Newfoundland, Canada, which is based on the first appearance datum (FAD) of *Treptichnus*  
70 *pedum* ichnospecies (Brasier et al., 1994), has been particularly problematic since it occurs in a  
71 section with few datable volcanics, sparse skeletal biota, and limited potential for

72 chemostratigraphy (Babcock et al., 2014). Indeed, the choice of *T. pedum* as a marker fossil for  
73 the basal Cambrian has also been a source of contention given the strong environmental,  
74 lithological and facies dependency for preservation of this trace, resulting in a notable absence  
75 from carbonate-dominated successions (e.g. Babcock et al., 2014). A similar problem is  
76 encountered when attempting to define the basal Cambrian using the first appearance of  
77 ‘Cambrian-type’ small skeletal fossils, which are themselves absent or rare in siliciclastic-  
78 dominated successions, especially in environments that were not conducive to early  
79 phosphatization. To overcome this complication, a holistic integration of radiometric,  
80 chemostratigraphic and palaeontological data across this interval is crucial. At present, the age of  
81 the Ediacaran-Cambrian boundary is  $541.0 \pm 1.0$  Ma (ICC 2021), however the radiometric age of  
82 a tuff deposit in the Nama Group, Namibia, on the Kalahari Craton, provides a current best estimate  
83 of 538.8 Ma for the maximum age of the first appearance of *T. pedum* (Linnemann et al., 2019;  
84 Xiao and Narbonne, 2020).

85 The carbon isotopic composition of marine carbonates ( $\delta^{13}\text{C}_{\text{carb}}$ ) is most commonly considered  
86 to reflect secular changes in the ratio of  $^{13}\text{C}$  to  $^{12}\text{C}$  in seawater that are associated with changes in  
87 the relative export/burial rates of inorganic versus organic carbon (Kaufman et al., 1991; Keith  
88 and Weber, 1964; Veizer et al., 1980; Veizer and Hoefs, 1976). As a result, secular  $\delta^{13}\text{C}_{\text{carb}}$  profiles  
89 have been used for regional and global correlation (Halverson et al., 2010; Macdonald et al., 2013;  
90 Maloof et al., 2010; Yang et al., n.d.; Zhu et al., 2007). However, a number of local effects have  
91 also been proposed that may partially decouple the local record of primary  $\delta^{13}\text{C}_{\text{carb}}$  from the  
92 composition of dissolved inorganic carbon (DIC) in the open ocean. These include diurnal  
93 coupling between photosynthesis and carbonate saturation in shallow carbonate settings (Geyman  
94 and Maloof, 2019), local DIC pools of distinct isotopic composition (Cui et al., 2020b; Melim et

95 al., 2002), and the possibility for water-column methanogenesis and carbonate recycling under  
96 low-sulfate conditions associated with restriction (Cui et al., 2020b). Additionally, facies-specific  
97 diagenetic regimes can yield distinct  $\delta^{13}\text{C}_{\text{carb}}$  for time-equivalent sections in modern marine basins  
98 (Melim et al., 2002), and this has also been established in the Cryogenian interglacial ocean  
99 (Hoffman and Lamothe, 2019), and the Paleoproterozoic Lomagundi-Jatuli event (Prave et al.,  
100 2021). As a result, changes in  $\delta^{13}\text{C}_{\text{carb}}$  may in fact archive contemporaneous pools of DIC from  
101 adjacent depositional settings with variable C isotope composition. The potential for both local  
102 water column DIC and the effects of carbonate diagenesis to result in significant deviation of  
103  $\delta^{13}\text{C}_{\text{carb}}$  from global seawater  $\delta^{13}\text{C}$  may therefore be problematic when building  $\delta^{13}\text{C}_{\text{carb}}$ -based age  
104 frameworks.

105 Despite these potential complications, it is not clear why during certain intervals of geological  
106 history some depositional settings acquire  $\delta^{13}\text{C}_{\text{carb}}$  values that deviate markedly from mean values  
107 (Hoffman and Lamothe, 2019). For example, integrated  $\delta^{13}\text{C}_{\text{carb}}$ ,  $\delta^{44}\text{Ca}$ ,  $\delta^{26}\text{Mg}$  and sequence  
108 stratigraphic study of the Cryogenian interglacial Trezona  $\delta^{13}\text{C}_{\text{carb}}$  excursion reveals that, whilst  
109 facies-specific trends in  $\delta^{13}\text{C}_{\text{carb}}$  may correspond with fluid vs sediment buffered diagenesis, the  
110 excursion itself is of global significance and may correspond with global changes in siliciclastic  
111 vs carbonate sedimentation, nutrient delivery, and eustatic sea level (Ahm et al., 2021). Therefore,  
112 notwithstanding uncertainties in the driving mechanisms for  $\delta^{13}\text{C}_{\text{carb}}$  records and possible facies-  
113 related, diagenetic offsets, the secular trends represented by gradual unidirectional shifts in  $\delta^{13}\text{C}_{\text{carb}}$   
114 in multiple globally distributed and temporally equivalent open-marine sections may reflect  
115 changes to the carbon cycle that are of global significance, and hence are applicable for  
116 chemostratigraphic correlation.

117 To date, efforts to produce a global composite Ediacaran  $\delta^{13}\text{C}_{\text{carb}}$  record (e.g. Macdonald et al.,  
118 2013; Yang et al., 2021) have revealed the middle Ediacaran Shuram negative anomaly at around  
119  $<579 - >564$  Ma (Rooney et al., 2020; Yang et al., 2021), followed by a positive shift from ca.  
120 564-550 Ma. The sedimentary record from ca. 564-550 Ma is radiometrically well dated in Baltica  
121 (the East European Platform) (Yang et al., 2021) and Avalonia (Matthews et al., 2020; Noble et  
122 al., 2015); however, siliciclastic strata with poor  $\delta^{13}\text{C}_{\text{carb}}$  resolution dominate these successions. A  
123 subsequent negative excursion with a recovery at  $\sim 550$  Ma (Yang et al., 2021) is followed by a  
124 final late Ediacaran positive plateau (the EPIP, Zhu et al., 2017). This plateau appears to terminate  
125 with the onset of a globally widespread large magnitude (min  $\delta^{13}\text{C}_{\text{carb}}$  of  $-10\%$ ) negative excursion,  
126 termed '1n' in strata of the Siberian Platform, and in previous global compilations (Kouchinsky et  
127 al., 2007; Maloof et al., 2010). This excursion is considered to be approximately coincident with  
128 the Ediacaran-Cambrian boundary and has also previously been termed the 'Basal Cambrian  
129 negative  $\delta^{13}\text{C}_{\text{carb}}$  excursion' (BACE); an acronym that is adopted herein. The age of the BACE is  
130 currently correlated with a radiometrically dated negative excursion in the A4 Member of the Ara  
131 Group, Oman at  $\sim 541$  Ma (Bowring et al., 2007; Hodgin et al., 2020; Maloof et al., 2010; Smith  
132 et al., 2015). Possible mass extinctions have been suggested between the Ediacaran White Sea and  
133 Nama biotic assemblages, and again at the Ediacaran-Cambrian boundary, coincident with the  
134 BACE (e.g. Amthor et al., 2003; Darroch et al., 2018).

135 Determining the global nature and age of the BACE has been particularly problematic, but is  
136 critical for developing a robust biostratigraphic and chronostratigraphic framework across this  
137 interval. The BACE reaches a  $\delta^{13}\text{C}_{\text{carb}}$  nadir of  $-10\%$  and has been recorded in all fossiliferous  
138 successions with high-resolution  $\delta^{13}\text{C}_{\text{carb}}$  data, except the Nama Group. The FAD of *T. pedum*  
139 occurs above the BACE in all regions that host both features (e.g. Smith et al., 2015, 2016; Hodgin

140 et al., 2020). As a radiometric basis for the age of the Ediacaran-Cambrian boundary derives from  
141 the Nama Group (Linnemann et al., 2019; Xiao and Narbonne, 2020), the position of the BACE  
142 (if present) in the Nama succession must be determined. Recent high precision radiometric and  
143  $\delta^{13}\text{C}_{\text{carb}}$  data from Laurentia appear to constrain the age of the BACE nadir to  $\leq 539.4$  Ma,  
144 coincident with stable positive  $\delta^{13}\text{C}_{\text{carb}}$  data on the Kalahari craton (Hodgin et al., 2020). It has  
145 therefore been suggested that the conflicting  $\delta^{13}\text{C}_{\text{carb}}$  trends between the Laurentian and Kalahari  
146 datasets may result from local pools of dissolved inorganic carbon (DIC) with distinct isotopic  
147 compositions (Hodgin et al., 2020). In order to test whether these data are unrepresentative of  
148 global  $\delta^{13}\text{C}_{\text{carb}}$ , it is first necessary to discount all alternative possibilities associated with  
149 uncertainties in the  $\delta^{13}\text{C}_{\text{carb}}$  age model framework.

150 Here, we present an updated  $\delta^{13}\text{C}_{\text{carb}}$  framework for the Ediacaran Nama Group of southern  
151 Namibia. These data are first correlated regionally by combined litho-, chemo-, and sequence  
152 stratigraphy, then constrained in time using published high precision U-Pb ages determined via  
153 zircon chemical abrasion isotope dilution thermal ionization mass spectrometry (CA-ID-TIMS).  
154 We correlate trends in the resulting Nama reference curve with  $\delta^{13}\text{C}_{\text{carb}}$  data from globally  
155 distributed sections that are well constrained by interbedded zircon U-Pb CA-ID-TIMS ages, and  
156 robust high-resolution regional section correlation, for the interval  $\sim 551 - 538.5$  Ma. The  $\delta^{13}\text{C}_{\text{carb}}$   
157 record is then extended to 517 Ma in multiple regions with high resolution litho-, chemo-, and  
158 sequence stratigraphic records. Compiled data from sections that host the most robust radiometric  
159 constraints throughout this interval act as framework curves to reveal trends in the global data that  
160 can be confidently constrained in age. These curves are used to anchor a wider correlation in order  
161 to best fit high-resolution  $\delta^{13}\text{C}_{\text{carb}}$  data from key sections that lack robust radiometric constraints.

162 This allows construction of four possible composite carbon isotope curves and age models,  
163 comprising 130 globally distributed sections (Australia, Brazil, Kazakhstan, Mongolia, Morocco,  
164 Namibia, Mexico, USA, Canada, Oman, Siberia and South China). These curves are consistent  
165 with all reliable radiometric age data and strontium isotope ( $^{87}\text{Sr}/^{86}\text{Sr}$ ) records between ~551 – 517  
166 Ma (Tables S1 and S2). All models reveal a previously underappreciated degree of variability in  
167 the EPIP, incorporating multiple positive and negative excursions preceding the BACE that are  
168 globally widespread. Differences between the four age models result from ongoing uncertainties  
169 which we review in detail. All FADs and, for Ediacaran taxa, Last Appearance Datums (LADs) of  
170 key fossil occurrences are calibrated within this framework (Tables S2 and S3). This provides the  
171 basis for biotic temporal and spatial distributions to be accurately constrained and visualized.

172

## 173 **2. Constructing a $\delta^{13}\text{C}_{\text{carb}}$ reference curve for the Nama Group, Kalahari Craton**

174 The Nama Group in Namibia and South Africa, comprises a richly-fossiliferous mixed  
175 carbonate-siliciclastic succession deposited in a foreland basin on the Kalahari Craton. The  
176 succession developed during flexural subsidence associated with two major orogenies; the Damara  
177 to the north, and the Gariiep to the southwest (Germs, 1983; Germs and Gresse, 1991; Gresse and  
178 Germs, 1993) (Fig. 1). Near-complete exposure and minimal structural deformation across  
179 hundreds of square kilometers have inspired half a century of detailed sedimentological and  
180 palaeontological research, incorporating high resolution litho-, chemo- and sequence stratigraphy  
181 (Darroch et al., 2015, 2016, 2021; Jensen et al., 2000; Saylor, 2003; Saylor et al., 1998; Smith,  
182 1998; Wood et al., 2015). These aspects, in combination with high-precision radiometric age  
183 calibration (Bowring et al., 2007; Grotzinger et al., 1995; Linnemann et al., 2019), make the Nama

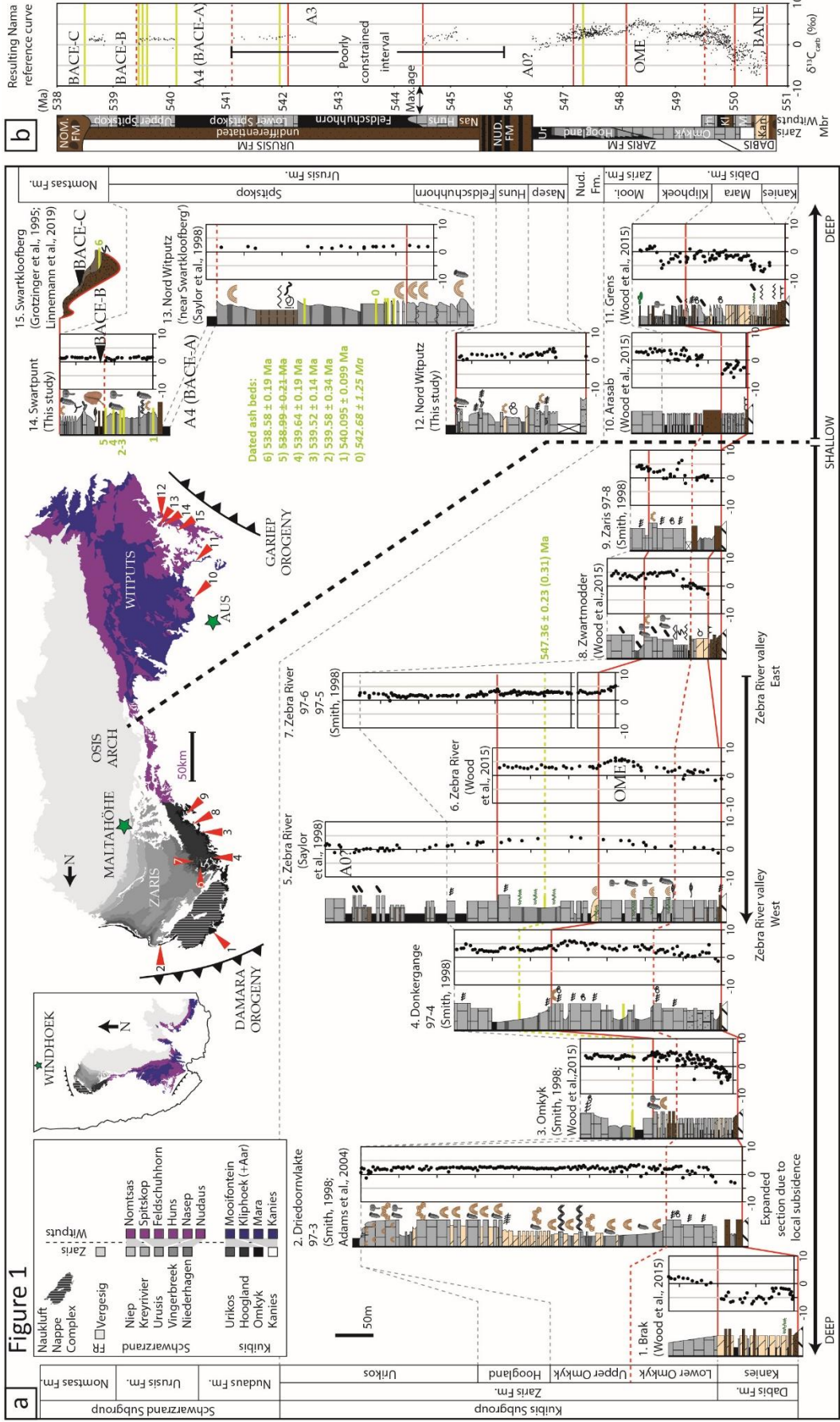


184 Group the best candidate succession globally for construction of a terminal Ediacaran  $\delta^{13}\text{C}_{\text{carb}}$   
185 reference curve. This is especially the case for the lower Nama Group (Kuibus Subgroup), where  
186 carbonate ramp deposits are ubiquitous throughout the northern (Zaris) sub-basin.

187  $\delta^{13}\text{C}_{\text{carb}}$  data from fifteen sections of the Nama Group, Namibia (Saylor et al., 1995; Smith,  
188 1998; Wood et al., 2015), compiled within a sequence stratigraphic framework and calibrated to  
189 dated volcanic tuff interbeds, result in a composite Ediacaran Nama  $\delta^{13}\text{C}_{\text{carb}}$  reference curve (Fig.  
190 1). Gaps in the  $\delta^{13}\text{C}_{\text{carb}}$  record of individual sections are permitted at exposure or erosion surfaces,  
191 or during significant intervals of siliciclastic deposition. Below, we explore implications for global  
192 correlation of the  $\delta^{13}\text{C}_{\text{carb}}$  reference curve derived for the Kuibus (ca. 551 – 546 Ma) and  
193 Schwarzrand (<546 – 538 Ma) subgroups.

## 194 *2.1 The Kuibus Subgroup*

195 In the Kuibus Subgroup succession, positive, laterally consistent  $\delta^{13}\text{C}_{\text{carb}}$  values in the lower  
196 Hoogland Member (Zaris Formation) of the Zaris sub-basin are constrained by a zircon U-Pb CA-  
197 ID-TIMS age of  $547.36 \pm 0.23$  Ma (Bowring et al., 2007) (Fig. 1). Carbonate strata in multiple  
198 sections below this ash bed record a gradual recovery from a negative  $\delta^{13}\text{C}_{\text{carb}}$  excursion. This can  
199 be readily correlated with the  $\delta^{13}\text{C}_{\text{carb}}$  trend expressed in strata of the lower Dengying Formation,  
200 South China. Recovery from this negative  $\delta^{13}\text{C}_{\text{carb}}$  excursion in the lower Dengying Formation is  
201 constrained by a zircon U-Pb CA-ID-TIMS age of  $550.1 \pm 0.6$  Ma (Yang et al., 2021, updated  
202 from  $551.09 \pm 1.02$  Ma, Condon et al., 2005) from an ash bed in the underlying Miaohu Member  
203 at Jijiawan (/Jiuqunao) section (Table S1). The age of the 0‰ crossing point in the lower Kuibus  
204 Subgroup can therefore be anchored to ~550 Ma. The preceding negative excursion ( $\geq 550$  Ma),



206 **Fig. 1. Sequence stratigraphic and carbon isotope chemostratigraphic correlation of the**  
207 **Nama Group, Namibia with resulting reference curve for the Kalahari craton for the interval**  
208 **~550 – 538.5 Ma** (Saylor et al., 1998; Smith, 1998; Wood et al., 2015). (a) Litho-, chemo- and  
209 sequence stratigraphic correlation for sections of the Zaris sub-basin after Smith (1998) and Wood  
210 et al. (2015). New data for sections 12 and 14. (b) Resulting Nama  $\delta^{13}\text{C}_{\text{carb}}$  reference curve showing  
211 position of tuff bed age constraints and sequence boundaries. Note that age model between ca. 547  
212 Ma and 540 Ma remains poorly constrained. BANE: Basal Nama Excursion, OME: Omkyk  
213 Excursion, A0, A3 and A4 named after tentative correlation with radiometrically dated excursions  
214 in the A0, A3 and A4 members of the Ara Group, Oman (see text for details). BACE-A, B and C  
215 correlate to the positions of the 1n/BACE in models A, B and C, respectively (Table S2). See Fig.  
216 2 for key to lithology and sequence stratigraphy. Radiometric data ( $^{238}\text{U}/^{206}\text{Pb}$  CA-ID-TIMS) are  
217 from (Bowring et al., 2007; Linnemann et al., 2019) and italicized data (air abrasion ID-TIMS  
218  $^{207}\text{Pb}/^{206}\text{Pb}$ ) are from Grotzinger et al. (1995) recalculated in Schmitz (2012) (the age of tuff bed  
219 5 is discounted; details in Table S1). See Fig. S1 for a high-resolution version of this figure.

220

221 whilst present and radiometrically calibrated in South China, is expressed most completely and  
222 with highest resolution in multiple sections by carbonates of the Dabis Formation in both the Zaris  
223 and Witputs sub-basins of the Nama Group. This is a recently recognized distinct negative  $\delta^{13}\text{C}_{\text{carb}}$   
224 excursion (Yang et al., 2021), herein termed the basal Nama excursion (BANE, Fig. 1b).

225 Subsequent to the BANE, peak  $\delta^{13}\text{C}_{\text{carb}}$  values are reached within the upper Omkyk Member of  
226 the Zaris Formation, and lower members of the Dengying Formation. This  $\delta^{13}\text{C}_{\text{carb}}$  peak is herein  
227 termed the Omkyk excursion (OME, Fig. 1b).

228 The onset of a gradual decline prior to  $547.32 \pm 0.31$  Ma (Bowring et al., 2007) is constrained  
229 by a tuff bed within the lower Hoogland Member of the upper Zaris Formation and correlative  
230 intervals of the lower Dengying Formation (Table S2). Declining  $\delta^{13}\text{C}_{\text{carb}}$  values culminate in a  
231 short-lived (<0.5 Ma) negative excursion, with a recovery to  $\sim 0\text{‰}$  recorded at  $546.72 \pm 0.21$  Ma  
232 by a tuff bed in the middle A0 Member of the Ara Group, Oman (see section 5.5, Bowring et al.,  
233 2007; Schmitz, 2012). This minor negative excursion is expressed in carbonate interbeds of the  
234 Urikos Member of the Zaris Formation, Namibia, and the A0 Member of the Ara Group, Oman  
235 (Bowring et al., 2007; Saylor et al., 1998). It may also correspond with a minor negative excursion  
236 recorded in the lower Khatyspyt Fm of the northern Siberian Platform (Cui et al., 2016; Knoll et  
237 al., 1995), although this remains uncertain (see section 5.3).

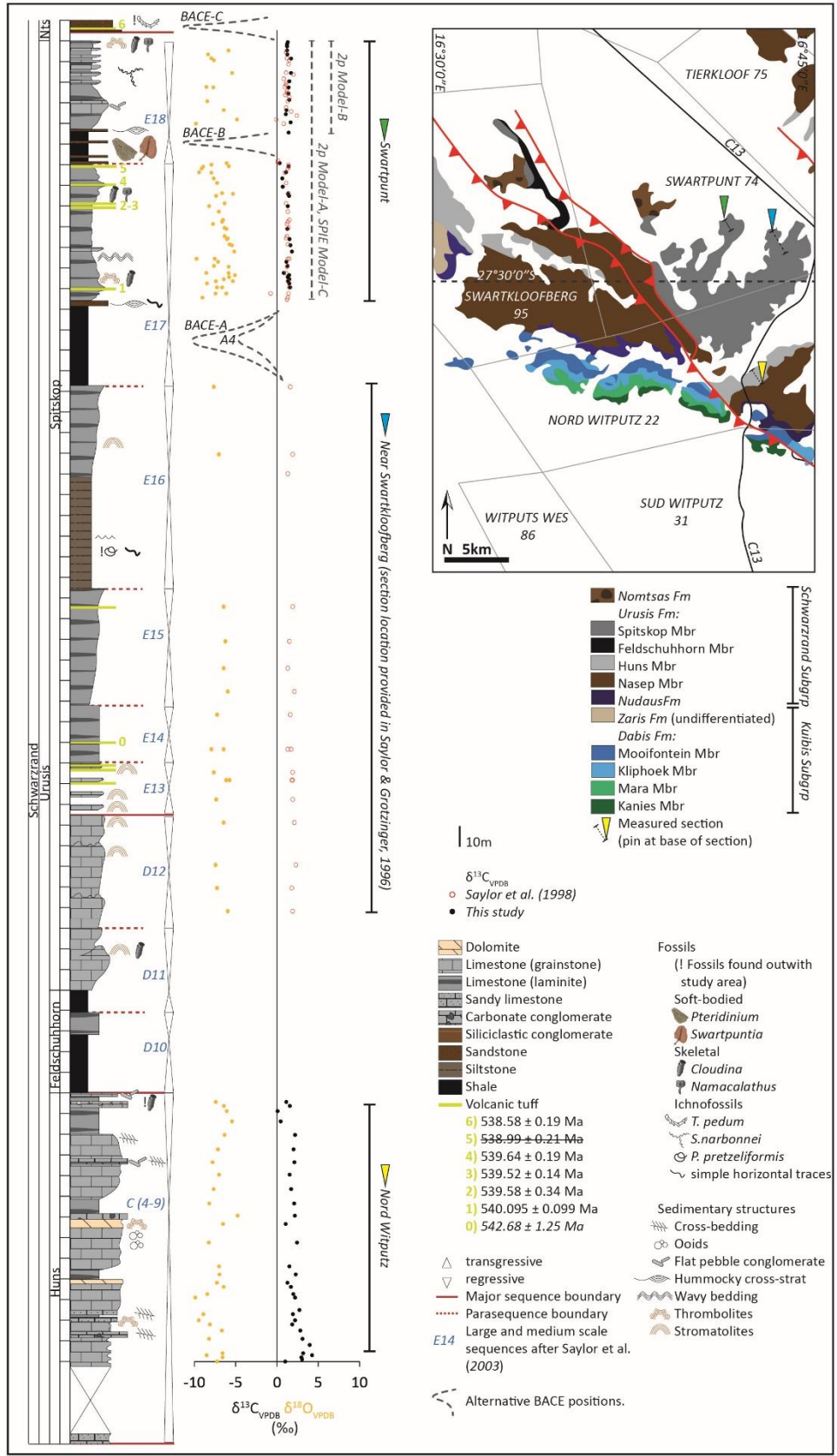
238 Based on the interbasinal  $\delta^{13}\text{C}_{\text{carb}}$  correlation herein (Fig. 1) and published palaeontological  
239 information, carbonates in the lower Kuibis Subgroup (Mara Member of the Dabis Fm) of the  
240 Witputs sub-basin host the earliest FAD of *Cloudina* (Germis, 1983). This FAD may predate the  
241  $0\text{‰}$  recovery from the BANE, however the precise location of the section that hosts the Mara  
242 Member cloudinids and associated  $\delta^{13}\text{C}_{\text{carb}}$  data is undocumented. In the Zaris sub-basin, the  
243 earliest recorded appearance of cloudinids occurs immediately above the  $0\text{‰}$  recovery from the  
244 BANE ( $\sim 550$  Ma) within the lowermost upper Omkyk Member (Fig. 1). Siliciclastics in the lower  
245 Kuibis Subgroup (Kliphoek Member of the Dabis Formation) of the Witputs sub-basin, deposited  
246 immediately below the  $0\text{‰}$  recovery from the BANE, contain a rich fossil archive of soft-bodied  
247 biota (Maloney et al., 2020). The majority of the soft-bodied fossils in this interval correspond to  
248 the Nama assemblage, however this level may also host the regional last appearance of elements  
249 of the White Sea assemblage, including *Ausia fenestrata* (Hahn and Pflug, 1985; Pickford, 1995).  
250 Fossil impressions interpreted as *Ausia* have previously been noted from the middle Verkhovka

251 Formation of the White Sea area (Grazhdankin, 2004), below a volcanic tuff in the overlying lower  
252 Zimnie Gory Formation recently redated to  $552.96 \pm 0.19$  (Yang et al., 2021) (Table S1).

## 253 *2.2 The Schwarzrand Subgroup*

254 During deposition of the Schwarzrand Subgroup the locus of carbonate sedimentation shifted  
255 to the Witputs sub-basin, and siliciclastic deposits of the Zaris sub-basin record gradual basin infill  
256 (Germs, 1983; Gresse and Germs, 1993). The existing  $\delta^{13}\text{C}_{\text{carb}}$  record of the Schwarzrand  
257 Subgroup consists of a low resolution  $\delta^{13}\text{C}_{\text{carb}}$  dataset from the Huns and lower Spitskop members  
258 of the Urusis Formation, and multiple datasets of varying resolution from the upper Spitskop  
259 Member at Farm Swartpunt (Linnemann et al., 2019; Saylor et al., 1998; Wood et al., 2015). We  
260 present new  $\delta^{13}\text{C}_{\text{carb}}$  data for two sections from the Urusis Fm (Nord Witputz and Swartpunt), and  
261 construct a composite lithostratigraphic and chemostratigraphic column incorporating available  
262 data from the lower Spitskop Member (Saylor et al., 1998) (Fig. 2).

263 Shallow marine facies of the lower Huns Member at Nord Witputz show initially high  $\delta^{13}\text{C}_{\text{carb}}$   
264 values (max = 4.24‰) that gradually decrease to reach 0.08‰ near the top of the section (Fig. 2).  
265 Higher order variability in the  $\delta^{13}\text{C}_{\text{carb}}$  data of the lower Huns Member may be associated with a  
266 series of parasequences, where lower  $\delta^{13}\text{C}_{\text{carb}}$  reflects deepening of the depositional environment.  
267 Samples of both shallow and marginally deeper facies show pronounced and simultaneous  
268 decreases in their mean  $\delta^{13}\text{C}_{\text{carb}}$  composition up-section, which may reflect a gradual trend in  
269 seawater  $\delta^{13}\text{C}_{\text{carb}}$  overprinted by minor perturbations associated with regional facies. Based on  
270 regional stratigraphic correlation, the Urusis Fm of the Witputs sub-basin was deposited equivalent  
271 to siliciclastic deposits of the Schwarzrand Subgroup in the Zaris sub-basin (Germs, 1983), and is  
272 therefore likely to be younger than ~546 Ma (Fig. 1).



274 **Fig. 2. Geological map and sampled sections of the Urusis Formation, Nama Group, southern**  
275 **Namibia.** Composite section after (Saylor, 2003). Geological map shows relative positions of  
276 measured sections. Map redrawn from Saylor and Grotzinger (1996) using the 1:250000 map of  
277 Ai-Ais (2716), Geological Survey of Namibia, Ministry of Mines and Energy. Radiometric data  
278 ( $^{238}\text{U}/^{206}\text{Pb}$  CA-ID-TIMS) are from Linnemann et al. (2019) and italicized data (air abrasion ID-  
279 TIMS  $^{207}\text{Pb}/^{206}\text{Pb}$ ) are from Grotzinger et al. (1995) recalculated in Schmitz (2012) (the age of tuff  
280 bed 5 is discounted; details in Table S1). BACE-A, B and C correlate to the positions of the  
281 1n/BACE in models A, B and C, respectively (Table S2).

282

283 The lower Spitskop Member contains a volcanic tuff deposit with a  $^{207}\text{Pb}/^{206}\text{Pb}$  age of 542.68  
284  $\pm 1.25$  Ma (Grotzinger et al., 1995, recalculated in Schmitz, 2012) (Table S1). Carbon isotope data  
285 of relatively low resolution have previously been presented for the lower Spitskop Member from  
286 the lower part of a composite section described as ‘near Swartkloofberg’ (Saylor et al., 1998) (Fig.  
287 2). The lower part of this section (corresponding to medium scale sequences D11 – E16 of Saylor,  
288 2003) lies to the north of our Huns Member section, and the upper part (medium scale sequences  
289 E17 and E18 of Saylor, 2003) corresponds to the Swartpunt section (Fig. 2, and see Fig. 1 of Saylor  
290 and Grotzinger, 1996). According to Saylor (2003), a total thickness of ~370 m of interbedded  
291 shale and carbonate, for which only 18 data points are currently published, separates the Huns  
292 Member at Nord Witputz from the upper Spitskop Member at Swartpunt (Fig. 2) (Saylor et al.,  
293 1998). However, an alternative correlation for the relative position of the lower Spitskop Member  
294 data is discussed in the Supplementary Information. Future high resolution resampling for  $\delta^{13}\text{C}_{\text{carb}}$ ,  
295 in addition to re-dating of ash beds throughout the lower Spitskop Member southeast of Swartpunt

296 using the updated CA-ID-TIMS methodology, should yield valuable information to better  
297 constrain this interval in the global age model.

298

### 299 **3. Developing Age Models and the stratigraphic position of the BACE in Namibia**

#### 300 *3.1 The terminal Ediacaran (546–541 Ma)*

301 The  $\delta^{13}\text{C}_{\text{carb}}$  record between 546 Ma and 543 Ma remains poorly constrained globally due to a  
302 dearth of  $\delta^{13}\text{C}_{\text{carb}}$  data interbedded with tuff beds dated by reliable radiometric methods (Fig. 3a).  
303 However, when the new  $\delta^{13}\text{C}_{\text{carb}}$  data of the Huns Member are compared to other  $\delta^{13}\text{C}_{\text{carb}}$  profiles  
304 from ca. 546–543 Ma from other cratons (e.g. Yangtze Block, Laurentia, Amazonia and Siberia,  
305 Fig. 3), the magnitude and overall trend in the data are consistent with a temporal position  
306 coincident with the initial downturn from positive values of up to 5‰ recorded in the middle  
307 Member of the Dengying Formation (Gaojiashan Member and equivalent units). We stress that  
308 this is a maximum age estimate based on the assumption that the age constraint from the overlying  
309 lower Spitskop Member ( $542.68 \pm 1.25$  Ma, Grotzinger et al., 1995, updated in Schmitz, 2012)  
310 approximates the true age of the lower Spitskop Member (see Supplementary Text for further  
311 discussion). A subsequent recovery to a positive  $\delta^{13}\text{C}_{\text{carb}}$  peak is well constrained by 5 radiometric  
312 ages;  $543.40 \pm 3.5$  Ma from the Baimatuo Member of the Yangtze Platform (Huang et al., 2020),  
313  $542.90 \pm 0.12$  Ma and  $542.33 \pm 0.11$  Ma from the lower and upper A3 Member of the Ara Group  
314 (Bowring et al., 2007), and  $542.37 \pm 0.28$  Ma and  $541.85 \pm 0.75$  Ma from the upper Tamengo  
315 Formation, Brazil (Parry et al., 2017). Here,  $\delta^{13}\text{C}_{\text{carb}}$  values increase once more to 3–5.6‰ (herein  
316 termed the ‘A3’ anomaly, Fig. 3) and then decline to a plateau of 0–2‰ prior to 541 Ma (Tables

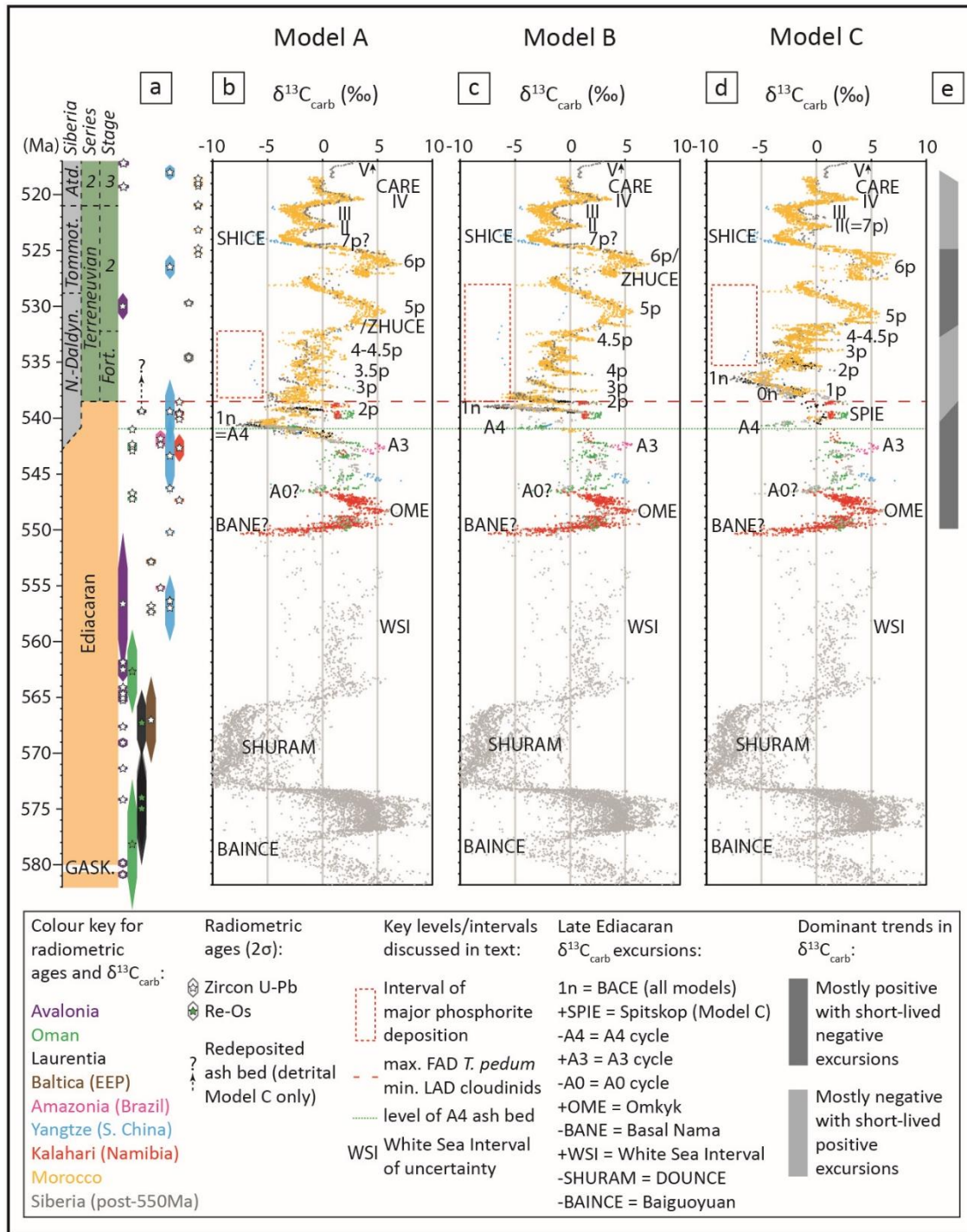


317 S1 and S2). The available data from the lower Spitskop Member, though sparse, correlate with  
318 predominantly positive  $\delta^{13}\text{C}_{\text{carb}}$  values that precede the negative excursion recorded in the A4  
319 Member of the Ara Group (Fig. 3).

320 There are three possible positions for the BACE in the Nama Group, all of which are consistent  
321 with available radiometrically-dated tuff deposits and occur in siliciclastic units without  $\delta^{13}\text{C}_{\text{carb}}$   
322 data (Fig. 2). These give rise to three alternative age models A, B and C (Fig. 3). In each, we  
323 assume that the age of the A4 Member accurately constrains the  $\delta^{13}\text{C}_{\text{carb}}$  excursion recorded in the  
324 A4 Member, as shown by Bowring et al. (2007) (see section 5.5 for further discussion of the Ara  
325 Group age model). For ease of distinction, the excursion in the A4 Member is herein termed the  
326 ‘A4 anomaly’. The position of the BACE in relation to the Spitskop Member is inferred either  
327 within the shale interval of medium scale sequence E17, stratigraphically beneath the ca. 540 Ma  
328 tuff bed at the base of the Swartpunt section (Model A), within the shale interval of medium scale  
329 sequence E18 above the well dated horizon constrained by multiple tuff deposits at ca. 539.6 Ma  
330 (Linnemann et al., 2019) (Model B), or in strata younger than the Swartpunt section (<538 Ma,  
331 Model C) (Figs. 2, 3).

332 Models A and B are consistent with a recent radiometric constraint from the La Ciénega  
333 Formation, Mexico (Hodgin et al., 2020). However, models B and C imply that the A4 anomaly  
334 does not correspond to the BACE, but rather to an earlier negative excursion with a recovery at or  
335 before ca. 540 Ma (Figs. 3c and d). In models A and B, the apparent absence of the BACE nadir  
336 in the Nama Group is interpreted simply as a function of coincident deposition of outer shelf shale  
337 for which  $\delta^{13}\text{C}_{\text{carb}}$  data are lacking (Fig. 2). Indeed, if the A4 anomaly is of global significance and

338



339

340 **Fig. 3. Carbon isotope chemostratigraphic correlation models A–C.** Ediacaran  $\delta^{13}\text{C}_{\text{carb}}$  data are  
 341 only presented for sections that are anchored by associated radiometric ages (e.g. Swartpunt), or  
 342 where high resolution  $\delta^{13}\text{C}_{\text{carb}}$  data are confidently correlated regionally to sections that contain  
 343 radiometrically dated beds (e.g. La Ciénega Fm and Kuibis Subgroup sections). All data are

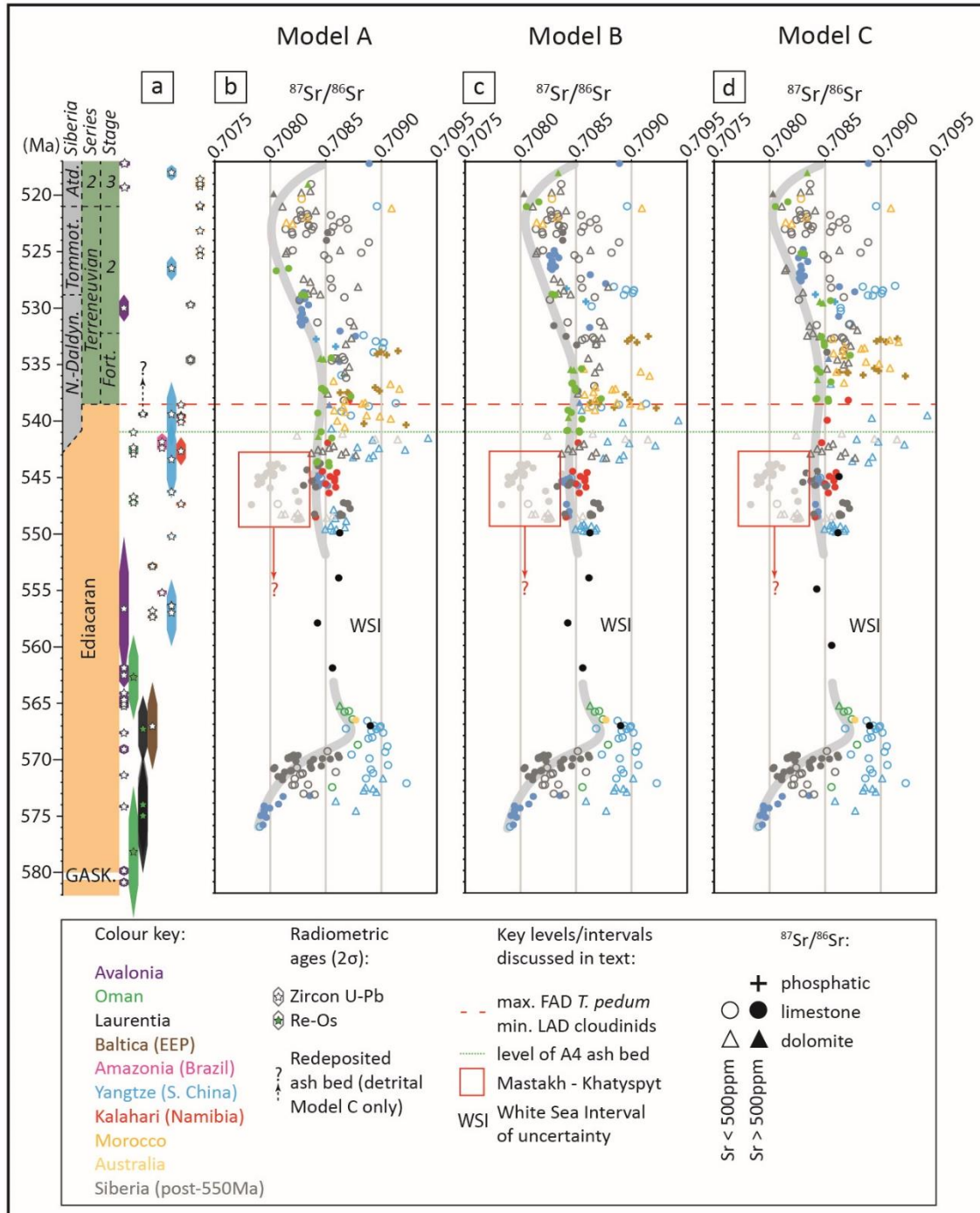
344 coloured by craton (or region). Age model for 582–550 Ma interval in grey after Yang et al. (2021).  
345 **(a)** Available radiometric ages with associated internal/analytical uncertainty. See Supplementary  
346 Materials (Tables S1 and S2) for references to radiometric and  $\delta^{13}\text{C}_{\text{carb}}$  data, in addition to  
347 biostratigraphic and section information. BANE marks the basal Nama negative  $\delta^{13}\text{C}_{\text{carb}}$  excursion,  
348 OME marks the positive  $\delta^{13}\text{C}_{\text{carb}}$  peak recorded in the Omkyk Member of the Zaris Formation of  
349 the Nama Group, Namibia. A0, A3 and A4 mark the relative positions of  $\delta^{13}\text{C}_{\text{carb}}$  excursions with  
350 radiometric ages in the Ara Group, Oman.  $\delta^{13}\text{C}_{\text{carb}}$  peaks 1p–6p, and II–V are labelled after direct  
351 correlation with the Sukharikha River section and Lena River sections of Siberia (e.g. Kouchinsky  
352 et al., 2007). 1n is equivalent to the BACE in all models.

353

354 correctly constrained in time (see section 5.5), it is sequestered within a shale interval  
355 stratigraphically beneath the Swartpunt section in all models.

### 356 *3.2 $^{87}\text{Sr}/^{86}\text{Sr}$ chemostratigraphy of the Ediacaran-Cambrian transition*

357 Matching  $\delta^{13}\text{C}_{\text{carb}}$  excursions in fossiliferous Ediacaran sections that display one or more  
358  $\delta^{13}\text{C}_{\text{carb}}$  excursions but lack radiometric ages is complicated by the finding here of multiple global  
359 late Ediacaran  $\delta^{13}\text{C}_{\text{carb}}$  excursions. This is equally problematic for the multiple excursions present  
360 in the Fortunian Stage of the lower Cambrian. In an attempt to address this issue, we compile a  
361 further database of published  $^{87}\text{Sr}/^{86}\text{Sr}$  data as an independent chronostratigraphic test (Table S2,  
362 Fig. 4). These  $^{87}\text{Sr}/^{86}\text{Sr}$  data have been screened on a case-by-case basis using available  
363 geochemical data to account for modification of the Sr isotope composition associated with  
364 diagenetic alteration or common Rb (see Supplementary Text, Table S2). Reliable  $^{87}\text{Sr}/^{86}\text{Sr}$  data



365

366 **Fig. 4. Sr isotope chemostratigraphy with associated radiometric ages (a) resulting from**

367 **carbon isotope chemostratigraphy after Model A (b), Model B (c) and Model C (d) for the**

368 **interval ~576–517 Ma.** Red boxes highlight unusually depleted values of the Mastakh and  
369 Khatyspyt formations. Data coloured according to craton (or region).

370

371 are anchored directly to the prescribed age of the corresponding  $\delta^{13}\text{C}_{\text{carb}}$  value in the same sample.  
372 In this way, we are able to constrain trends that we consider the most robust estimate of seawater  
373  $^{87}\text{Sr}/^{86}\text{Sr}$  composition, and use  $^{87}\text{Sr}/^{86}\text{Sr}$  as an independent chronostratigraphic indicator for age  
374 models A, B and C for sections that lack radiometric ages (Fig. 4).

375 Revision of the age of the Shuram excursion after Rooney et al. (2020) and Yang et al. (2021)  
376 results in a highly uncertain interval ('WSI' in Figs. 3, 4) where  $^{87}\text{Sr}/^{86}\text{Sr}$  data are largely  
377 unconstrained with the possible exception of values corresponding to the Blueflower Formation of  
378 NW Canada (Narbonne et al., 1994). The resulting late Ediacaran  $^{87}\text{Sr}/^{86}\text{Sr}$  record (~551 – 538  
379 Ma) is characterized by values that are relatively invariant about 0.70842–0.70846, and these  
380 values are consistent between Namibia, South China, Mongolia and southeastern Siberia (Table  
381 S2). The Khatyspyt Formation yields inconsistent outlier values down to 0.70784 (boxed data in  
382 Fig. 4b-d), accompanied by a high degree of scatter in  $\delta^{13}\text{C}_{\text{carb}}$ . The position of the Khatyspyt  
383 Formation remains problematic due to uncertainties in the nature of the boundary with the  
384 overlying Turkut Formation (see section 5.3). However, we consider the correlation proposed  
385 herein to be a reasonable estimate based on consistent  $\delta^{13}\text{C}_{\text{carb}}$  trends between the Khatyspyt  
386 Formation and globally distributed sections throughout this interval.  $^{87}\text{Sr}/^{86}\text{Sr}$  values remain  
387 constant throughout much of the Fortunian, but begin to decline approximately coincident with  
388 rising  $\delta^{13}\text{C}_{\text{carb}}$  values in Cambrian Stage 2, reaching a nadir of ~0.70805 near the boundary between  
389 stages 2 and 3, prior to gradual recovery during upper Stage 3.

### 390 3.3 Incorporating additional section data

391 In order to test the validity of our Nama reference curve for global  $\delta^{13}\text{C}_{\text{carb}}$  correlation, and to  
392 explore the three alternative age models, we expand our dataset to incorporate published data from  
393 correlative strata into the early Cambrian from other cratons and regions (e.g. Yangtze Block,  
394 Oman, Laurentia, Amazonia, Morocco, Siberia, Mongolia, Fig. 3). We first prioritise sections with  
395  $\delta^{13}\text{C}_{\text{carb}}$  data and interbedded volcanic deposits dated via zircon U-Pb CA-ID-TIMS. Values of  
396  $\delta^{13}\text{C}_{\text{carb}}$ , anchored by the age of interbedded tuff deposits (within internal/analytical uncertainty)  
397 provide the scaffold for wider correlation, and intervals that lack constraint from radiometric ages  
398 are considered to be the most uncertain (Tables S1 and S2). Within this framework, we utilize  
399 regional sequence stratigraphic models that incorporate gaps in the carbon isotope record of  
400 individual sections, due to unconformities or intervals of siliciclastic deposition, while excluding  
401 unreasonable sedimentation rates for given tectonic settings (Table S2). Individual sections are  
402 subdivided into units of consistent lithofacies, and relative sedimentation rates are permitted to  
403 vary accordingly (Table S2). Deeper marine carbonate facies (e.g. organic-rich thinly bedded  
404 limestone laminae) and intervals of phosphorite deposition typically exhibit lower rates of  
405 deposition than shallow marine carbonate facies (e.g. dolostone and oolitic limestone deposited  
406 above fair weather wave base) within each region (Table S2).

407 Several high resolution  $\delta^{13}\text{C}_{\text{carb}}$  correlation frameworks have been assembled for the lower  
408 Cambrian (e.g. Brasier et al., 1994; Knoll et al., 1995; Kouchinsky et al., 2017, 2007, 2005; Maloof  
409 et al., 2010; Smith et al., 2015, Table S2). Our new framework is consistent with that derived by  
410 Maloof et al., (2010), but updates their model through incorporation of more recent high resolution  
411  $\delta^{13}\text{C}_{\text{carb}}$  datasets (e.g. Kouchinsky et al., 2017; Smith et al., 2015) and radiometric constraints (e.g.

412 Hodgin et al., 2020; Landing et al., 2020; Linnemann et al., 2019). We also consider updated  
413 biostratigraphic information integrated with  $\delta^{13}\text{C}_{\text{carb}}$  from sections in South China (Steiner et al.,  
414 2020), Australia (Betts et al., 2018) and Laurentia (Dilliard et al., 2007).

415 All global  $\delta^{13}\text{C}_{\text{carb}}$  correlation models reveal widespread, but short-lived, negative excursions  
416 in an interval dominated by positive  $\delta^{13}\text{C}_{\text{carb}}$  values in the terminal Ediacaran ~551–538 Ma (Fig.  
417 3e). These models differ most prominently in their correlation of the BACE nadir, either within  
418 the latest Ediacaran (models A and B) or within the lowermost Cambrian (Model C), as defined  
419 by its position relative to the radiometric age that currently constrains the FAD of *T. pedum* in  
420 Namibia (Fig. 3). However, *T. pedum* has not been reported in strata older than the BACE nadir in  
421 any region that hosts the BACE, and so the BACE nadir may in fact be older than the Ediacaran-  
422 Cambrian boundary in all models (discussed further below). Models B and C offer valid  
423 alternatives to the generally accepted Model A that are consistent with radiometric (models B and  
424 C) and stratigraphic (Model C) information in all regions. The relative likelihood of each of these  
425 three models, and their biostratigraphic implications, are further discussed below.

426

#### 427 **4. Implications for the age of the BACE and the Ediacaran-Cambrian boundary**

428 The A4 anomaly records minimum  $\delta^{13}\text{C}_{\text{carb}}$  values of -5‰ and one outlier value of -6.7‰  
429 (Amthor et al., 2003; Bowring et al., 2007) (Figs. 3 and 5). The onset of this negative excursion is  
430 anchored by an age of  $541.00 \pm 0.13$  Ma (Bowring et al., 2007). The overlying A5 Member of the  
431 Ara Group records stable positive values of 2-3‰, prior to the onset of another negative excursion  
432 (Amthor et al., 2003). The radiometric age of the A4 Member has been used to constrain an onset  
433 age for the BACE of ~541 Ma (Model A, e.g. Bowring et al., 2007; Hodgin et al., 2020; Linnemann

434 et al., 2019; Maloof et al., 2010). As previously noted, the BACE reaches a nadir of -10‰ and is  
435 recorded in all fossiliferous successions with high-resolution  $\delta^{13}\text{C}_{\text{carb}}$  data, except the Nama Group,  
436 Namibia (Figs. 3 and 5, Table S2). A maximum age of  $539.40 \pm 0.23$  Ma derives from a sandy  
437 dolostone bed in the La Ciénega Formation, Mexico, which lies within negative  $\delta^{13}\text{C}_{\text{carb}}$  values  
438 inferred to correspond to the BACE interval (Tables S1 and S2, Hodgins et al., 2020). However,  
439 strata of the upper Spitskop Member of the Urusis Formation (Nama Group, southern Namibia) at  
440 the Swartpunt section record relatively stable positive  $\delta^{13}\text{C}_{\text{carb}}$  values about 1‰ that are consistent  
441 with values from the A5 Member and constrained by 4 high resolution tuff bed ages between ca.  
442 540 Ma and 539.5 Ma (Figs. 2, 3, 5, Table S1) (Linnemann et al., 2019).

443 In Model A (Fig. 3b), the A4 anomaly and BACE are equivalent and constrained below the  
444 Swartpunt section in the shale interval of medium scale sequence E17 (Fig. 2). In this model, the  
445 BACE onset is at ca. 541 Ma, constrained in the A4 Member, and the recovery occurs at or before  
446 540 Ma, constrained at the base of Swartpunt section. This is also consistent with the interpreted  
447 depositional age being close to the radiometric age determined for the sandy dolostone bed in the  
448 La Ciénega Fm, Mexico (Hodgins et al., 2020). However, this implies that 1) the clastic unit that  
449 hosts the sandy dolostone bed was deposited at a slower depositional rate above the BACE nadir,  
450 2) the BACE recovery and plateau recorded at Swartpunt are constrained within the clastic horizon  
451 of the La Ciénega Fm and are therefore not recorded, and 3) a second more minor negative  
452 excursion is recorded above the level of the dolostone bed (possibly equivalent to the onset of 2n  
453 or a preceding minor negative excursion).

454 In Model A, positive  $\delta^{13}\text{C}_{\text{carb}}$  values in the uppermost Spitskop Member at Swartpunt may  
455 correlate with the 2p interval in Siberia (Kouchinsky et al., 2007), Mongolia (Smith et al., 2015)



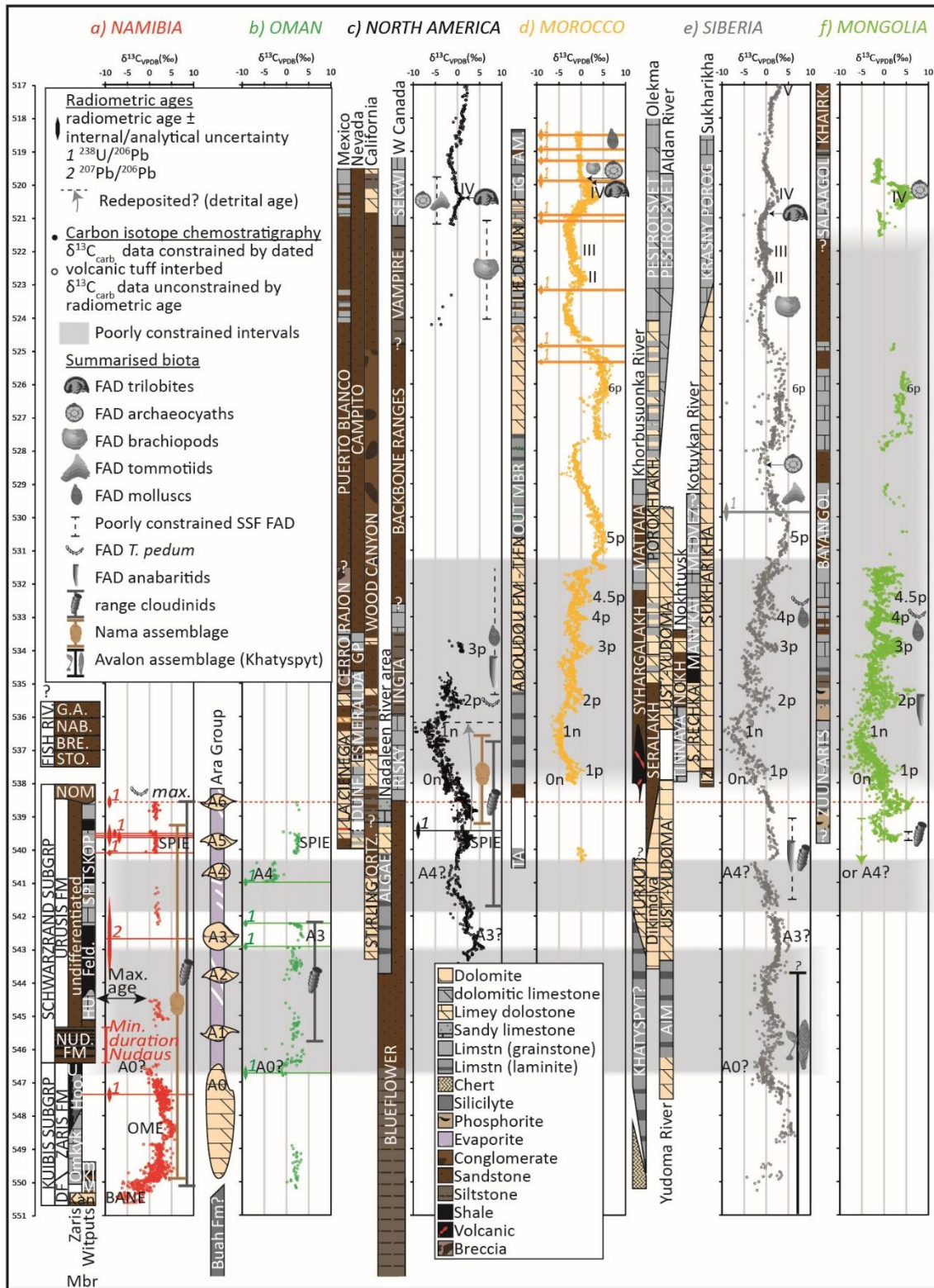
456 and possibly Morocco (Maloof et al., 2010), all of which postdate the BACE nadir (Fig. 3b).  
457 However, in all areas that host high-resolution Fortunian  $\delta^{13}\text{C}_{\text{carb}}$  records, peaks 2p-4.5p appear to  
458 be short-lived positive excursions in an interval dominated by negative mean  $\delta^{13}\text{C}_{\text{carb}}$  values (Fig.  
459 3e). The duration of the 2p interval implied by the Swartpunt radiometric data therefore appears  
460 to contradict the best-fit  $\delta^{13}\text{C}_{\text{carb}}$  correlations of Fortunian sections (Maloof et al., 2010),  
461 notwithstanding the possibility for stratigraphic condensation in other regions at the 2p level (Figs.  
462 3b and e). We consider the caveats associated with the La Ciénega Fm correlation and  
463 inconsistencies relating to inferred peak duration between Swartpunt and 2p to make Model A less  
464 likely than models B or C for the BACE position, although it remains possible.

465 By contrast, models B and C imply that the A4 anomaly and BACE are two distinct excursions,  
466 with nadirs that are separated from one another by up to 5 million years (Figs. 3-5). In Model B  
467 (Fig. 3c) a return to positive  $\delta^{13}\text{C}_{\text{carb}}$  values following the A4 anomaly is constrained by the age of  
468  $540.095 \pm 0.099$  Ma at the base of the Swartpunt section, Namibia (Fig. 2) (Linnemann et al.,  
469 2019). The BACE onset occurred after  $\sim 539.6$  Ma, as constrained by three radiometric ages from  
470 the Swartpunt section immediately below carbonates that record a decrease in  $\delta^{13}\text{C}_{\text{carb}}$  to 0‰ (Figs.  
471 2 and 3c, Table S1, Linnemann et al., 2019), which is consistent with the aforementioned  
472 radiometric constraint of 539.4 Ma from the La Ciénega Formation, Mexico (Hodgin et al., 2020).  
473 In this model, recovery from the BACE in Namibia occurred prior to  $\sim 538.6$  Ma, consistent with  
474 a likely minimum age for the uppermost Spitskop Member at Swartpunt, as constrained by an ash  
475 bed age within the overlying Nomtsas Formation at a neighboring section (Linnemann et al., 2019)  
476 (Figs. 1 and 2). Although this model is consistent with all radiometric constraints, it implies that  
477 the BACE was a very short-lived event on the order of 1 Myr. This model demands that some  
478 sections (e.g. Sukharikha River) exhibited significantly higher sedimentation rates during the

479 BACE (1n) interval than the overlying 2p-5p interval, which appears inconsistent with the  
480 relatively monotonous lithofacies documented throughout.

481 Figure 5 presents age Model C for selected successions that host the highest resolution  $\delta^{13}\text{C}_{\text{carb}}$   
482 data for the critical late Ediacaran to Cambrian Stage 3 (Atdabanian) interval, in regions without  
483 significant Fortunian phosphorite deposition. Sections in Morocco, the Zavkhan terrane of  
484 Mongolia, and the Siberian Platform have limited Ediacaran-Fortunian radiometric ages, and  
485 therefore rely upon best-fit  $\delta^{13}\text{C}_{\text{carb}}$  correlation throughout this interval. In Model C (Figs. 3d and  
486 5), the onset of the BACE is inferred to post-date the Swartpunt section (<538.5 Ma). Stable  
487 positive  $\delta^{13}\text{C}_{\text{carb}}$  values in the interval ~540 – 539.5 Ma, as constrained at Swartpunt, separate the  
488 A4 anomaly from the BACE with the resulting peak herein termed the Spitskop excursion (SPIE,  
489 Figs. 3d and 5). Model C implies that 1) the A4 anomaly is distinct from the BACE, and 2) the age  
490 derived from the La Ciénega Formation (Hodgin et al., 2020) is best interpreted as detrital (Fig.  
491 5). In this model, the sandy dolostone bed in the La Ciénega Formation was deposited up to 3 Myr  
492 after eruption of the incorporated tuffaceous material based on best fit with the  $\delta^{13}\text{C}_{\text{carb}}$  curve and  
493 constant average rates of sedimentation.

494 Figure 5 also shows that age-calibrated stratigraphy in many successions record a striking  
495 regional lithostratigraphic transition across the Ediacaran-Cambrian boundary interval. In many  
496 regions, the transition is marked by a widespread erosive unconformity or exposure surface (e.g.  
497 Namibia, NE Siberia), and/or a subsequent change in dominant lithofacies which may reflect  
498 changes in global sea level. Whilst invoking a eustatic driver for combined litho- and  
499 chemostratigraphic variability across this transitional interval is complicated by regional tectonics,  
500 this may have significant biostratigraphic implications that warrant future consideration.



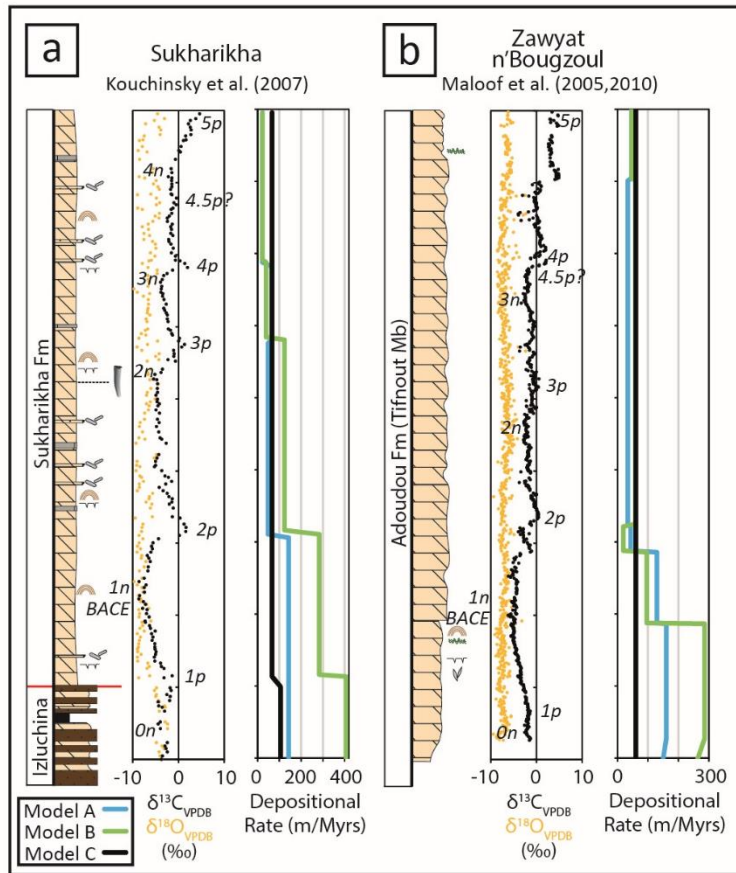
502 **Fig. 5. High-resolution age model correlation by region for Model C only.** Grey shading  
503 represents intervals of greatest uncertainty (see text for details). As in Fig. 3, the excursion marked  
504 as 1n represents the BACE. See Fig. S2 for a high resolution version of this figure.

505

506 Model C is our preferred correlation when considering best fit between sections that host  
507 continuous Fortunian  $\delta^{13}\text{C}_{\text{carb}}$  data, whereby dominantly negative  $\delta^{13}\text{C}_{\text{carb}}$  values are interrupted by  
508 short-lived positive excursions (Kouchinsky et al., 2007; Maloof et al., 2010) (e.g. Morocco,  
509 Siberia, Figs. 3d, e and 6). This model also permits a short-lived pre-BACE excursion (herein  
510 termed 0n) which is recorded in sections with high-resolution  $\delta^{13}\text{C}_{\text{carb}}$  data from Morocco (e.g.  
511 Oued Sdas and Oued n'Oulili sections, Maloof et al., 2005), Siberia (Sukharikha and Nokhtuysk  
512 sections, Kouchinsky et al., 2007; Pelechaty, 1998), Mongolia (Zavkhan terrane, Smith et al.,  
513 2015), and possibly Laurentia (Hodgin et al., 2020; Smith et al., 2016) (Figs. 5 and 6).

514 Model C also maintains near constant sedimentation rates in multiple Fortunian – Stage 2  
515 sections (Table S2). Taking two of the most continuous carbonate successions known with limited  
516 facies variation, Sukharikha River, Siberian Platform, and Zawyat n'Bougzoul, Morocco, we show  
517 that while Models A and B both show markedly declining sedimentation rates in both successions,  
518 Model C maintains a constant sedimentation rate (Fig. 6). At the resolution of lithostratigraphic  
519 detail afforded for each of these sections in the published literature, Model C appears to be the  
520 simplest and most parsimonious solution.

521 The maximum age for the regional FAD of *T. pedum* on the Kalahari Craton is associated with  
522 the radiometric age of the lower Nomtsas Formation, Namibia (Linnemann et al., 2019). We note,



523

524 **Fig. 6. Changes in sedimentation rate implied by models A to C for selected sections that**  
 525 **capture the BACE and show limited facies variation through continuous carbonate**  
 526 **successions. (a) Sukharikha River section (Igarka-Norilsk Uplift, Siberian Platform) and (b)**  
 527 **Zawyat n'Bougzoul section (Anti-Atlas, Morocco), with lithostratigraphy and  $\delta^{13}\text{C}_{\text{carb}}$  after**  
 528 **Kouchinsky et al. (2007) and Maloof et al. (2005), respectively. See Fig. 2 for key to lithology and**  
 529 **sequence stratigraphy.**

530

531 however, that *T. pedum* has not been reported from the section (Farm Swartkloofberg, Linnemann  
 532 et al., 2019) from which this radiometric age is derived. Instead, the FAD of *T. pedum* is reported  
 533 from entirely siliciclastic valley fill deposits of the Nomtsas Formation on Farms Sonntagsbrunn

534 and Vergelee, >100 km to the east of Farm Swartkloofberg (Table S3). By contrast, the FAD of *T.*  
535 *pedum* in Laurentia is well constrained above the nadir of the BACE recorded in carbonate  
536 interbeds of the Esmeralda Member of the Deep Spring Formation, Nevada (Fig. 5c, Smith et al.,  
537 2016). If Model C is correct, then the integrated  $\delta^{13}\text{C}_{\text{carb}}$  chemostratigraphy and biostratigraphy of  
538 the Mount Dunfee section may imply a far younger age for the FAD of *T. pedum* (~535.5 Ma),  
539 and by extension the Ediacaran-Cambrian boundary, than currently defined (Fig. 5). This may  
540 therefore also support a case for repositioning the Ediacaran-Cambrian GSSP to the Mount Dunfee  
541 section based on the best-fit calibration of the FAD of *T. pedum*.

542

## 543 **5. Ongoing uncertainties and biostratigraphic constraints**

544 The process of constructing these age models has exposed the largest remaining uncertainties  
545 in late Ediacaran – early Cambrian stratigraphic correlation, which occur mainly due to insufficient  
546 radiometric control. Despite these uncertainties, we build on the biostratigraphic framework of  
547 Maloof et al. (2010) and constrain the FADs of key Cambrian-type small skeletal fossil groups  
548 within each age model (Table S2).

### 549 *5.1 The possibility for a multimodal $\delta^{13}\text{C}_{\text{carb}}$ record*

550 High resolution  $\delta^{13}\text{C}_{\text{carb}}$  and sequence stratigraphic assessment of Cryogenian and early  
551 Ediacaran carbonates of the Congo Craton has revealed significant facies-dependency in the  
552 expression of presumed-global  $\delta^{13}\text{C}_{\text{carb}}$  excursions (Hoffman and Lamothe, 2019). In their model,  
553 Hoffman & Lamothe (2019) propose that the observed multimodal  $\delta^{13}\text{C}_{\text{carb}}$  expression between  
554 inner platform, basin margin and upper foreslope carbonates may be associated with significant  
555 facies-dependent distinction relating to seawater vs sediment-buffered diagenesis. They note that

556 this may significantly complicate the utility of  $\delta^{13}\text{C}_{\text{carb}}$  chemostratigraphic studies throughout  
557 geological time, especially where radiometric anchor-points are absent or sparse. Anomalously  
558 positive  $\delta^{13}\text{C}_{\text{carb}}$  values of the middle Bambuí Group of Brazil, stratigraphically above *Cloudina*-  
559 bearing carbonates, also clearly demonstrate offset from global seawater composition (Uhlein et  
560 al., 2019). This offset is interpreted to reflect local effects of unusual water column chemistry that  
561 likely result from partial restriction (Cui et al., 2020b; Uhlein et al., 2019).

562 In our models, a number of regions show a degree of scatter in  $\delta^{13}\text{C}_{\text{carb}}$ , with possible evidence  
563 for deviation from the idealized seawater  $\delta^{13}\text{C}_{\text{carb}}$  curve. Examples include the Zuun-Arts and  
564 Salaany Gol formations (Mongolia), and potential  $\delta^{13}\text{C}_{\text{carb}}$  bimodality between different facies  
565 across the Yangtze Block (South China). In particular, the negative excursions at ca. 546.5 Ma  
566 (A0) and 541 Ma (A4), which may be globally widespread, are significantly muted in sections of  
567 the Yangtze Block. Whether the excursions themselves, or the muted record in South China, best  
568 reflect true changes in seawater composition as opposed to degrees of diagenetic alteration or  
569 restriction, remains uncertain.

570 Resolving the possible multimodal nature of Ediacaran and lower Cambrian  $\delta^{13}\text{C}_{\text{carb}}$  records  
571 will benefit from future radiometric calibration, in addition to high-resolution studies of integrated  
572 stratigraphic, petrographic,  $\delta^{44/40}\text{Ca}$  and  $\delta^{26}\text{Mg}$  analyses (e.g. Ahm et al., 2021; Bold et al., 2020).  
573 Whilst this frustrates the utility of the proposed global  $\delta^{13}\text{C}_{\text{carb}}$  correlation for regional  
574 chemostratigraphic studies of unfossiliferous strata with limited radiometric constraints  
575 throughout this time interval, we note that it does not alter proposed FADs and LADs of key taxa.  
576 We tentatively suggest that the broad trends observed in  $\delta^{13}\text{C}_{\text{carb}}$  represented by gradual,  
577 unidirectional shifts in  $\delta^{13}\text{C}_{\text{carb}}$ , are consistent between sections but that the absolute magnitude of

578 positive and negative excursions may differ depending on the specifics of local diagenetic  
579 alteration and/or steepness of the local isotopic gradient of seawater during organic carbon  
580 remineralisation. We note that this assumption holds true even for the Cryogenian interglacial  
581 interval, with the possible exception of the interval recording the Taishir anomaly (Hoffman and  
582 Lamothe, 2019). In this regard, and given the stratigraphic alternatives considered herein (Fig. 2),  
583 we do not consider the stable, positive  $\delta^{13}\text{C}_{\text{carb}}$  data of the Swartpunt section to necessarily correlate  
584 with the nadir of the BACE, as has previously been suggested (e.g. Hodgin et al., 2020).

## 585 *5.2 Age of the base of the Dengying Formation*

586 In models A to C, the shape of the global composite  $\delta^{13}\text{C}_{\text{carb}}$  curve between ~547 Ma and 543  
587 Ma is dictated in large part by the age of the base of the Dengying Fm of the Yangtze Platform,  
588 South China, and the shape of the Dengying Fm  $\delta^{13}\text{C}_{\text{carb}}$  profile. Detailed litho-, chemo-, and  
589 sequence stratigraphic studies of the Ediacaran Yangtze Platform are numerous (e.g. An et al.,  
590 2015; Condon et al., 2005; Cui et al., 2016; Cui et al., 2019; Ishikawa et al., 2008; Li et al., 2013;  
591 Lu et al., 2013; Tahata et al., 2013; Wang et al., 2014, 2017; Yang et al., 2021; C. Zhou et al.,  
592 2017b; Zhu et al., 2007, 2013). A summary description of the Dengying Fm, and detailed section  
593 correlation figures (Figs. S3 and S4) are provided herein for reference.

594 The Dengying Fm is lithostratigraphically subdivided into three members, each of which have  
595 differing names that correspond to geographic position on the Yangtze Platform (Fig. S3). The  
596 lower Member is dominated by dolostone that was deposited during a sea level highstand atop  
597 black shale of Member IV of the Doushantuo Formation (Zhu et al., 2007). This unit corresponds  
598 to the Algal Dolomite and Donglongtan members on the shallow Yangtze platform to the north  
599 and west, respectively, where it reaches thicknesses of >280m. In the Yangtze Gorges area to the  
600 east, the equivalent Hamajing Member ranges in thickness from 3-60m in sections measured for



601  $\delta^{13}\text{C}_{\text{carb}}$  (Fig. S3), but may reach a maximum thickness of 200m (Jiang et al., 2007; Zhu et al.,  
602 2007).

603 A sequence boundary separates dolostone of the lower Dengying Fm from overlying  
604 fossiliferous deeper marine deposits of the middle Dengying Fm across the Yangtze Platform (Zhu  
605 et al., 2007). In the north, this unit corresponds to fossiliferous transgressive siliciclastics and  
606 limestones of the Gaojiashan Member (20-45m) (Cui et al., 2016; Cui et al., 2019; Zhu et al.,  
607 2007). Equivalent transgressive deposits of the middle Dengying Fm correspond to shale of the  
608 Jiucheng Member (20-45m) in the west, and bituminous limestone of the richly fossiliferous  
609 Shibantan Member (up to >100m) in the Yangtze Gorges area to the east (Duda et al., 2016; Xiao  
610 et al., 2020; Zhu et al., 2007).

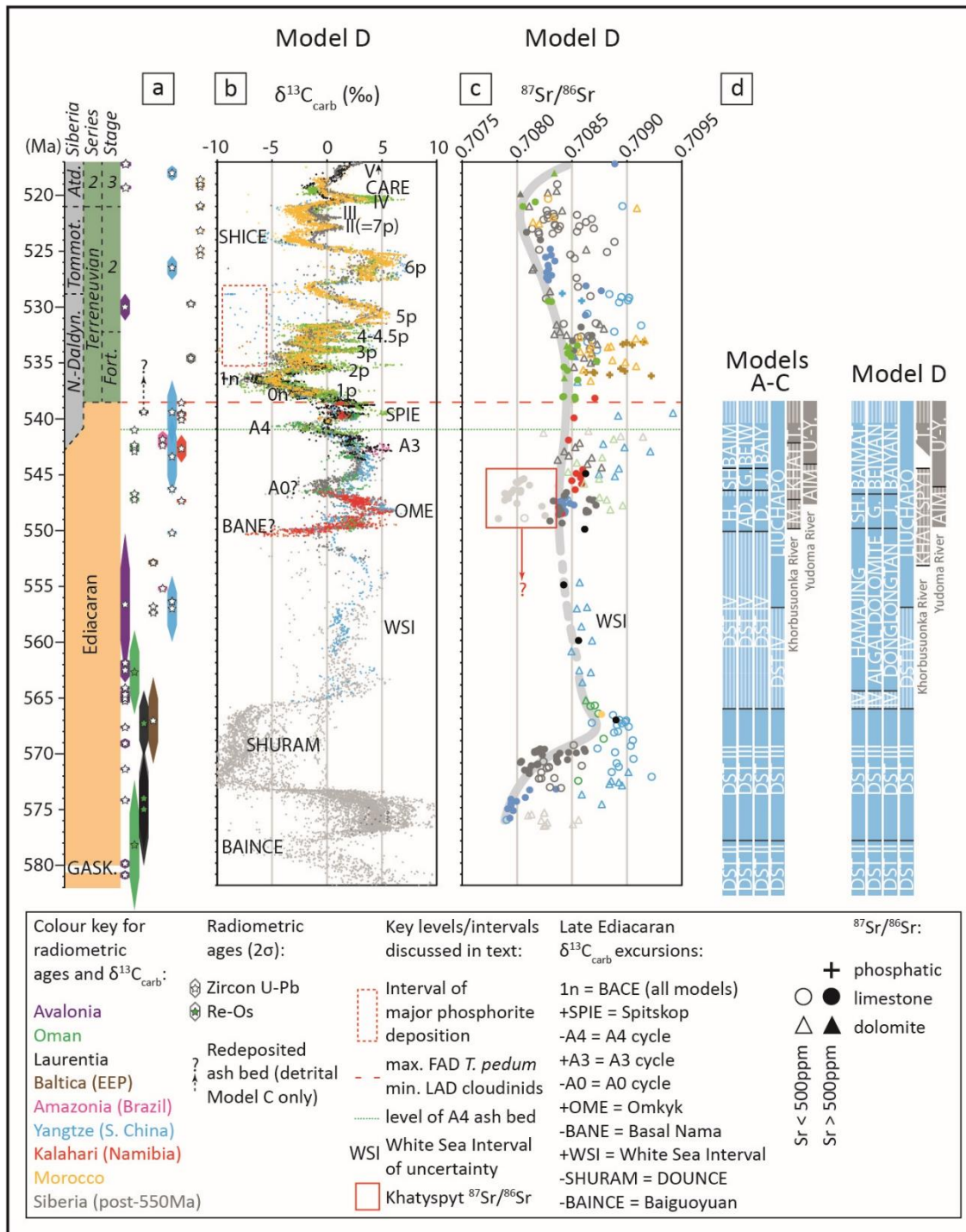
611 The third and topmost Member of the Dengying Fm is composed of highstand systems tract  
612 dolostones, which are frequently capped by a sequence boundary that shows evidence for  
613 exposure. In the north and west, this unit corresponds to the Beiwan (25-370m) and Baiyanshao  
614 ( $\leq 120\text{m}$ ) members, respectively, which correlate with the Baimatuo Member ( $\leq 400\text{m}$ ) in the  
615 Yangtze Gorges area (Zhu et al., 2007). Zircons within an ash layer 45m above the base of the  
616 Baimatuo Member at the Zhoujiaao section (central south Huangling anticline, Fig. S1) have been  
617 dated by U-Pb SIMS to  $543.40 \pm 3.5$  Ma (Huang et al., 2020).

618 A zircon U-Pb CA-ID-TIMS age of  $550.14 \pm 0.63$  Ma (Yang et al., 2021) from an ash bed at  
619 the top of Member IV (Miaohe Member) of the Doushantuo Fm at Jiuqunao section of the western  
620 Huangling anticline (Fig. S3) is classically considered to constrain a maximum age for the base of  
621 the Dengying Fm (Condon et al., 2005). The Dengying Fm in the Jiuqunao section records  
622 recovery from a negative  $\delta^{13}\text{C}_{\text{carb}}$  excursion characterised by increasing  $\delta^{13}\text{C}_{\text{carb}}$  from  $-4.05\text{‰}$  to  
623  $+3.56\text{‰}$  in  $<3\text{m}$  of dolostone (Fig. S3) (Condon et al., 2005; Yang et al., 2021; Zhu et al., 2007).

624 Unfortunately, lithostratigraphic and chemostratigraphic correlation between sections of the  
625 western Huangling anticline at the boundary between the Doushantuo and Dengying formations is  
626 complicated by slumping and associated stratigraphic repetition (Fig. S3) (An et al., 2015; Vernhet,  
627 2007; Yang et al., 2021; Zhou et al., 2017). Furthermore, the ~550 Ma ash layer at Jiuqunao section  
628 has not been reported at the top of Doushantuo Member IV, or elsewhere, from any other section  
629 on the Yangtze Platform to date.

630 Here we consider a further alternative model (Model D) that explores the implications of  
631 correlating the  $\delta^{13}\text{C}_{\text{carb}}$  data above the 550 Ma ash bed at Jiuqunao with the upper Hamajing Mb,  
632 rather than the basal Hamajing Mb (Fig. S4). In this model, the 550 Ma ash layer represents the  
633 age of slumping in the western Huangling anticline, and was deposited at the top of the disrupted  
634 unit, thereby permitting a conformable contact between the ash horizon and the overlying  
635 Dengying Fm at Jiuqunao section. The sequence stratigraphic framework for the entire Dengying  
636 Fm in sections across the Yangtze Platform and slope presented by Zhu et al. (2007) is maintained  
637 in Model D. However, this model implies that the thick Algal Dolomite and Donglongtan  
638 members, and the Hamajing Mb in many sections of the central and eastern Huangling anticline,  
639 were deposited between  $\leq 565$  Ma and ~550 Ma, rather than  $< 550$  Ma.

640 The alternative correlation presented in Model D greatly simplifies the global  $\delta^{13}\text{C}_{\text{carb}}$  curve  
641 between 546 Ma and 543 Ma and, by extension, between 550 Ma and 541 Ma (Fig. 7). In models  
642 A-C, the  $\delta^{13}\text{C}_{\text{carb}}$  profile from the (e.g.) Gaojiashan Member occupies the interval from 546 Ma to  
643 543 Ma, however in Model D the middle Member of the Dengying Fm across the Yangtze Platform  
644 correlates well with the  $\delta^{13}\text{C}_{\text{carb}}$  profile of the Kuibis Subgroup of the Nama Group, between 550



645

646 **Fig. 7. Model D output resulting from correlation of the ~550 Ma ash layer at the Jiuqunao**

647 **section with the upper Hamajing Mb and equivalent units of the lower Dengying Fm (see**

648 **Fig. S4). Age model from 541-517 Ma is consistent with Model C, and age model for 582–550**

649 **Ma interval in grey after Yang et al. (2021).** **A)** Radiometric ages with associated  $2\sigma$  uncertainty,  
650 **B)** Global  $\delta^{13}\text{C}_{\text{carb}}$  profile resulting from Model D correlation, **C)** Global  $^{87}\text{Sr}/^{86}\text{Sr}$  profile resulting  
651 from Model D correlation, **D)** Summary of differences in stratigraphic correlation between models  
652 A-C and Model D for stratigraphy of South China (blue) and Siberia (grey). SH = Shibantan, G =  
653 Gaojiashan, J = Jiucheng, BAIMAT = Baimatuo, BAIYAN = Baiyanshao, M = Mastakh, T =  
654 Turkut, U'-Y = Ust'-Yudoma.

655  
656 Ma and 546 Ma. Model D also implies that the Aim and Khatyspyt formations of the Siberian  
657 Platform may similarly occupy the interval from 550 Ma to 546 Ma based on best fit with the  
658 resulting global  $\delta^{13}\text{C}_{\text{carb}}$  curve (Fig. 7d). In Model D, the global  $\delta^{13}\text{C}_{\text{carb}}$  curve between 546.5 Ma  
659 and 541 Ma is characterised by a simple increase and decrease (Fig. 7b), from A0 to A3 and  
660 culminating in the A4 excursion (which may or may not correspond with the BACE).

### 661 5.3 Age of the Khatyspyt Formation

662 The temporal placement of the Khatyspyt Formation of the Olenek Uplift is key to  
663 understanding the degree of assemblage overlap between the Avalon, White Sea and Nama  
664 assemblages, as it contains typical Avalon assemblage fossils including the rangeomorphs *Charnia*  
665 *masoni* and *Khatyspytia grandis* (e.g. Cui et al., 2016). The age of the Khatyspyt Formation also  
666 has significant implications for the evolution and morphological changes in macroalgae during the  
667 late Ediacaran (Bykova et al., 2020). The Khatyspyt Formation has long been assumed to record  
668 deposition between ca. 560 and 550 Ma, approximately contemporaneously with the Miaohé  
669 Member and fossiliferous deposits of the White Sea area (e.g. Cui et al., 2016). In fact, the only  
670 radiometric constraint available is a maximum age for intrusion of the volcanic breccia of the Tas-

671 Yuryakh volcanic complex within the lower part of the Syhargalakh Formation (lower Kessyusa  
672 Group), which unconformably overlies the Khatyspyt and overlying Turkut formations. The  
673 maximum age for intrusion of this unit is  $542.8 \pm 1.30$  Ma, provided by zircon U-Pb air abrasion  
674 ID-TIMS (Table S1) (Bowring et al., 1993; Maloof et al., 2010; Rogov et al., 2015).  
675 Notwithstanding uncertainties in this age (Table S1), the Turkut Formation, which overlies the  
676 Khatyspyt Formation, contains the local FAD of the anabaritid *Cambrotubulus decurvatus* and the  
677 onset of a negative excursion which may be equivalent either to the A4 anomaly or the BACE  
678 (depending on the preferred model, Figs. 3 and 4). Screened  $^{87}\text{Sr}/^{86}\text{Sr}$  data for the Khatyspyt  
679 Formation (boxed data in Fig. 4b-d) are notably depleted (mean = 0.708038, n = 19, Cui et al.,  
680 2016; Vishnevskaya et al., 2017, 2013) relative to all screened data prior to the nadir in upper  
681 Cambrian Stage 2 (Table S2). Recent efforts to produce a global late Ediacaran  $^{87}\text{Sr}/^{86}\text{Sr}$   
682 compilation suggest that the low  $^{87}\text{Sr}/^{86}\text{Sr}$  data recorded by the Khatyspyt Formation are supportive  
683 of a temporal placement approximately coincident with and postdating data from the Nama Group  
684 (Cui et al., 2020a). Potential issues with this correlation are outlined below.

685 Carbon isotope data from the Nama Group are anchored at various levels to high precision  
686 radiometric ages (e.g. Bowring et al., 2007; Linnemann et al., 2019), and reveal trends in  $\delta^{13}\text{C}_{\text{carb}}$   
687 that are correlatable in other, globally distributed and similarly temporally well-constrained  
688 sections (e.g. Ara Group, Oman, Amthor et al., 2003; Bowring et al., 2007). Robust  $^{87}\text{Sr}/^{86}\text{Sr}$  data  
689 from the Nama Group are recorded from samples spanning the Omkyk Member (Zaris Formation)  
690 to the Nomtsas Formation, with relatively invariable  $^{87}\text{Sr}/^{86}\text{Sr}$  values (mean = 0.708538, n = 11)  
691 (Kaufman et al., 1993). Furthermore, high Sr limestones from the Shibantan Member, South China  
692 and the Zuun-Arts and overlying Bayan-Gol formations of the Zavkhan Terrane, Mongolia, show  
693 robust  $^{87}\text{Sr}/^{86}\text{Sr}$  values and  $\delta^{13}\text{C}_{\text{carb}}$  trends consistent with the record from the Nama Group, with

694 the latter extending relatively stable values of  $\sim 0.708500$  into the lower Fortunian (Fig. 4b-d, Table  
695 S2, Brasier et al., 1996). In light of available robust  $\delta^{13}\text{C}_{\text{carb}}$  and  $^{87}\text{Sr}/^{86}\text{Sr}$  data from radiometrically  
696 well-constrained sections, our compilation suggests either: 1) that low  $^{87}\text{Sr}/^{86}\text{Sr}$  values and an  
697 Avalon-type biotic assemblage support an older temporal placement for the Khatyspyt Formation  
698 than that shown in our compilation ( $>551$  Ma and possibly as old as  $\sim 575$  Ma), or 2) that the  
699  $^{87}\text{Sr}/^{86}\text{Sr}$  data recorded by the Khatyspyt Formation are not representative of global seawater  
700 composition. The nature of the contact between the Khatyspyt and Turkut formations along the  
701 Khorbusuonka River is key to determining the true placement of the Khatyspyt Formation, and  
702 reports vary considerably. For example, Cui et al. (2016) report that the boundary between the  
703 Khatyspyt and Turkut formations is conformable, whereas Vishnevskaya et al. (2017) suggest that  
704 this is an unconformable contact. However, neither publication provides figured evidence of the  
705 nature of the contact.

706 In our correlation, we tentatively assume that the hiatus (if any) at the boundary between these  
707 two formations along the Khorbusuonka River is relatively minor ( $<500$  kyrs). This is justified in  
708 part by the consistency in  $\delta^{13}\text{C}_{\text{carb}}$  and lithostratigraphy between late Ediacaran sections of the  
709 Olenek uplift and the Nama and Ara groups (Figs. 3 and 5). However, we stress that this requires  
710 future clarification due to the unusually low  $^{87}\text{Sr}/^{86}\text{Sr}$  data of the Khatyspyt Formation in this time  
711 interval. If the boundary is conformable, the presence of Avalon-type fossils in the Khatyspyt  
712 Formation, in addition to *Charniodiscus* noted from the Shibantan Member (Chen et al., 2014),  
713 together suggest that rare remnants of the Avalon assemblage remained until possibly as late as  
714 ca. 545.5 Ma. It is noteworthy that ordination plots of the overall late Ediacaran fossil assemblages  
715 have not placed the Khatyspyt assemblage within the Avalon-type biotas and instead place it with  
716 the younger White Sea biota (Boag et al., 2016). The temporal overlap between the Avalon and

717 Nama assemblages also holds true regardless of the age of the Khatyspyt Formation, as the age of  
718 the Shibantan Member is confidently constrained (< ca. 551 Ma) by the aforementioned  
719 radiometric age of the volcanic tuff deposit in the underlying upper Miaohe Member (Condon et  
720 al., 2005; Schmitz, 2012; Yang et al., 2021).

#### 721 *5.4 Age of the Turkut Formation:*

722 A maximum age for intrusion of the Tas-Yuryakh volcanic breccia within the lower  
723 Syhargalakh Formation (lower Kessyusa Group) along the Khorbusuonka River is suggested by a  
724 zircon U-Pb air abrasion ID-TIMS age of  $542.8 \pm 1.30$  Ma (Table S1) (Bowring et al., 1993;  
725 Maloof et al., 2010; Rogov et al., 2015). The intrusive Tas-Yuryakh volcanic breccia  
726 unconformably overlies the Turkut Formation. The FAD of the anabaritid *Cambrotubulus*  
727 *decurvatus* is recorded from the lower Turkut Formation in this section (Rogov et al., 2015), which  
728 supports a late Ediacaran lower boundary for the regional Nemakit-Daldynian Stage of Siberia,  
729 consistent with biostratigraphy and  $\delta^{13}\text{C}_{\text{carb}}$  chemostratigraphy in sections along the Yudoma River  
730 of SE Siberia (Zhu et al., 2017).  $\delta^{13}\text{C}_{\text{carb}}$  chemostratigraphic and sequence stratigraphic studies  
731 support temporal placement of the Turkut Formation of the Khorbusuonka River correlative with  
732 the middle – upper Ust'-Yudoma Formation in sections along the Yudoma River (Knoll et al.,  
733 1995; Pelechaty, 1998; Pelechaty et al., 1996b, 1996a; Zhu et al., 2017). Indeed, if the age of the  
734 Tas-Yuryakh volcanic breccia is close to the minimum age within analytical uncertainty, then the  
735 negative excursion recorded at the top of the Turkut Formation (Knoll et al., 1995) is equivalent  
736 to the A4 anomaly, and either corresponds with (Model A) or precedes (models B and C) the  
737 BACE. In both scenarios, the lower Turkut Formation and middle Ust'-Yudoma Formation at  
738 Kyra-Ytyga contain the earliest known FADs of anabaritids globally ( $\geq 541$  Ma, Fig. 8). It is likely

739 that future high precision CA-ID-TIMS analyses significantly alter the temporal position of the  
740 Tas-Yuryakh volcanic breccia, and by extension the minimum age of the underlying Turkut  
741 Formation. In the age models presented herein, a maximum age for the FAD of SSFs of the  
742 *Anabarites trisulcatus* – *Protohertzina anabarica* Zone (and by extension the Nemakit-Daldynian  
743 lower boundary) is therefore set at ca. 541–542 Ma across the Siberian Platform (Fig. 8). This  
744 temporal placement is most consistent with the dominant  $\delta^{13}\text{C}_{\text{carb}}$  trends observed pre-BACE,  
745 whereby positive  $\delta^{13}\text{C}_{\text{carb}}$  values are interrupted by short-lived negative excursions (Fig. 3e).

#### 746 *5.5 Integrated geochronology of the Ara Group*

747 A complication inherent in the chemostratigraphic assessment of the Ara Group is the nature  
748 of the carbonate units themselves, which are found as ‘stringers’, frequently interbedded by  
749 evaporite (Amthor et al., 2003; Bowring et al., 2007). We note that whilst the high precision  
750 radiometric ages provided by Bowring et al. (2007) confidently place these carbonate units in  
751 relative stratigraphic order, the analysed tuffaceous material and  $\delta^{13}\text{C}_{\text{carb}}$  datasets do not always  
752 derive from the same core. For example, the A0  $\delta^{13}\text{C}_{\text{carb}}$  excursion is recorded within the Sabsab-  
753 1 well, whereas the radiometric constraint of ~546.72 Ma derives from a tuff bed in the Asala-1  
754 well.  $\delta^{13}\text{C}_{\text{carb}}$  data for the Asala-1 well remain unpublished, precluding confident calibration of this  
755  $\delta^{13}\text{C}_{\text{carb}}$  excursion. Indeed, the only two wells for which both radiometric and  $\delta^{13}\text{C}_{\text{carb}}$  data are  
756 available are BB-5 and Minha-1. Whilst BB-5 constrains the A4 anomaly, Minha-1 captures  
757 positive  $\delta^{13}\text{C}_{\text{carb}}$  values in the A3 Member that are in agreement with radiometrically constrained  
758  $\delta^{13}\text{C}_{\text{carb}}$  data from Brazil (Parry et al., 2017) and South China (Huang et al., 2020).



759 We note that some other globally-distributed sections record an excursion that is demonstrably  
760 pre-BACE (e.g. Zuun-Arts Formation), which may be more consistent with an earlier, distinct ‘A4’  
761 anomaly. The A5 Member of the Ara Group also records a  $\delta^{13}\text{C}_{\text{carb}}$  plateau of similar magnitude  
762 to that recorded at Swartpunt (Figs. 5a, b), followed by a gradual decrease in  $\delta^{13}\text{C}_{\text{carb}}$  that mirrors  
763 the decrease seen above the level of the ca. 539.6 Ma horizon at Swartpunt (Figs. 2 and 5a, b).  
764 These features may add credence to a pre-BACE ‘A4’ anomaly (models B and C).

#### 765 *5.6 $\delta^{13}\text{C}_{\text{carb}}$ correlation of the lower Fortunian*

766 Recent biostratigraphic and  $\delta^{13}\text{C}_{\text{carb}}$  chemostratigraphic assessment of Ediacaran – Cambrian  
767 transitional strata of the Yangtze Platform, South China have shown a previously underappreciated  
768 level of  $\delta^{13}\text{C}_{\text{carb}}$  variability in the post-BACE, pre-ZHUCE (Zhujiaping positive  $\delta^{13}\text{C}_{\text{carb}}$  excursion)  
769 interval (Steiner et al., 2020). In age models A and B, the BACE is constrained to be late Ediacaran  
770 in age, with a nadir either at ca. 541 (Model A) or ca. 539 Ma (Model B, Figs. 3 and 9, Table S2).  
771 In Model C, the BACE is within the basal Cambrian based on correlation with the radiometric age  
772 and inferred maximum FAD of *T. pedum* in the Nomtsas Fm (Fig. 10). However, as noted above,  
773 the FAD of *T. pedum* is constrained to be post-BACE in all successions that host the BACE, which  
774 may also support an Ediacaran age for the BACE in Model C. The BACE is well-recorded in  
775 sections across the Yangtze Platform, South China, in the lower Zhujiaping Formation (Daibu  
776 Member) and Yanjiahe Formation, and is commonly overlain by phosphorus-rich carbonates of  
777 the middle Zhujiaping Formation (Zhongyicun Member) and equivalent units (Brasier et al., 1990;  
778 Steiner et al., 2020). Phosphorite deposition is globally widespread in lower Fortunian strata (e.g.  
779 Tarim, Yangtze Platform, Malyi Karatau of Kazakhstan, northern Mongolia, some sections of  
780 Laurentia), with carbonate substituted in the phosphorite lattice commonly recording very

781 negative, or highly variable  $\delta^{13}\text{C}_{\text{carb}}$  values that diverge from global seawater composition. The  
782 upper Yanjiahe Formation, above the level of the BACE, yields highly variable  $\delta^{13}\text{C}_{\text{carb}}$  values  
783 alongside SSFs of the *A. trisulcatus* – *P. anabarica* assemblage Zone (Steiner et al., 2020). The  
784 Kuanchuanpu Formation yields similarly variable  $\delta^{13}\text{C}_{\text{carb}}$  values and SSFs (Steiner et al., 2020; B.  
785 Yang et al., 2016). Crucially, the lower Kuanchuanpu Formation records the co-occurrence of  
786 *Cloudina* with SSFs of the *A. trisulcatus* – *P. anabarica* Zone (B. Yang et al., 2016), however the  
787 exact position of this mixed assemblage relative to the BACE nadir remains uncertain.

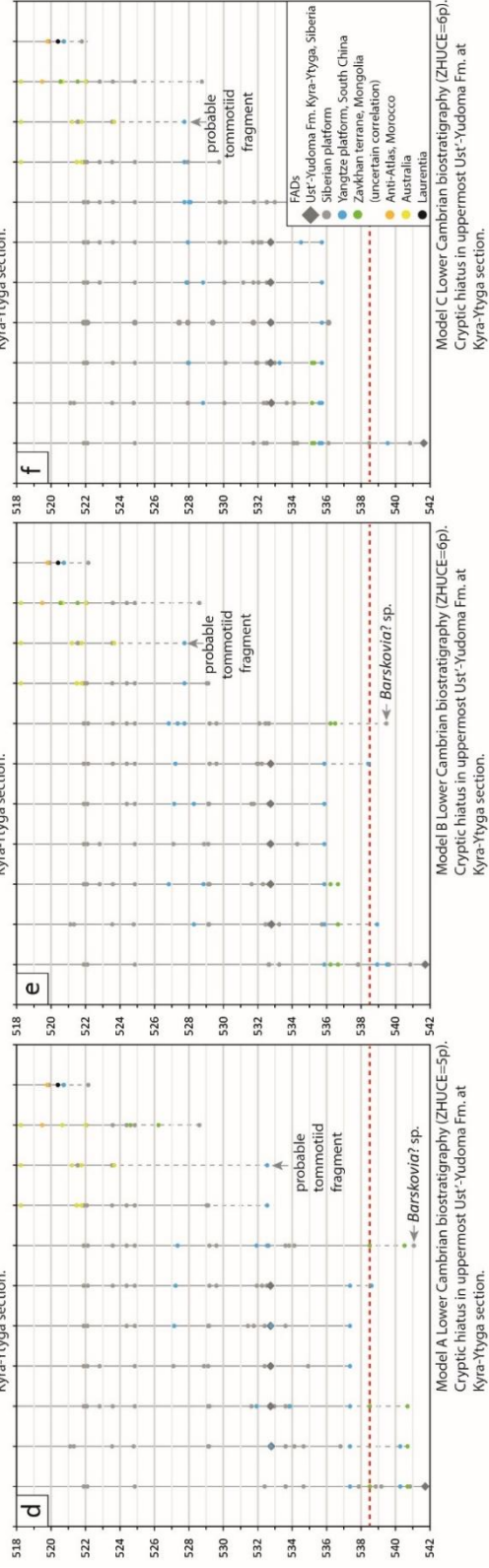
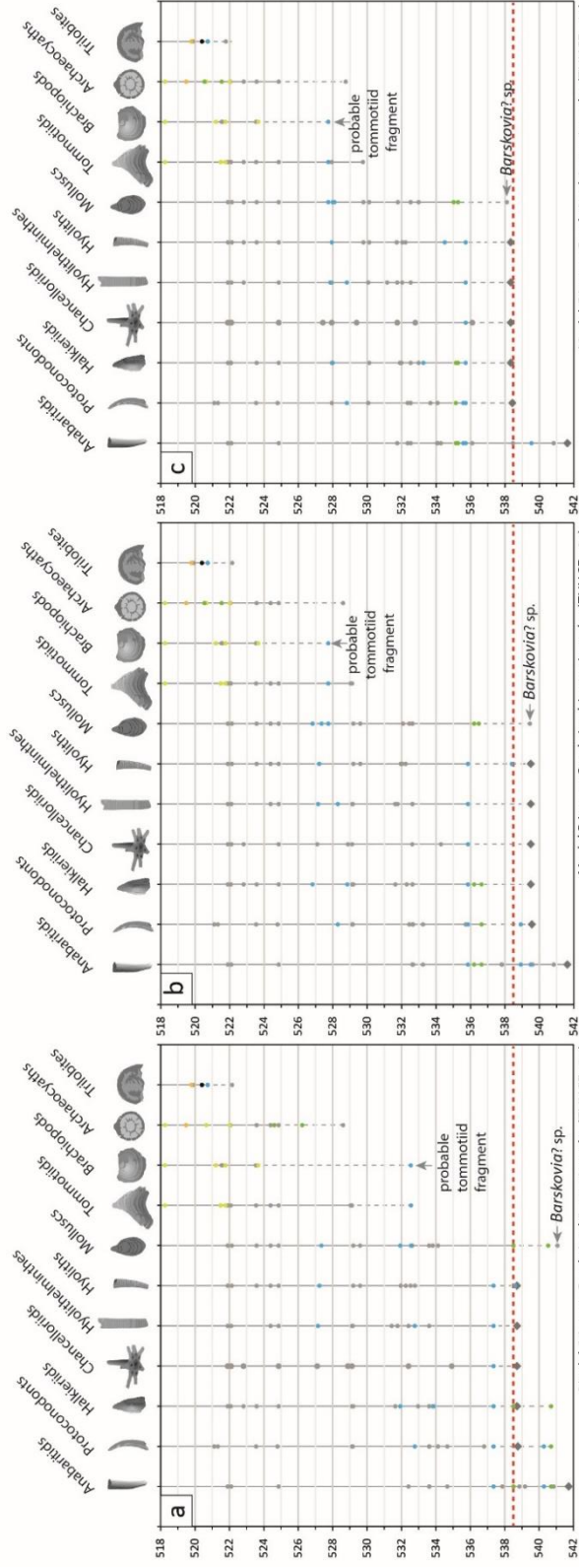
788 In areas where phosphorite deposition is limited, the  $\delta^{13}\text{C}_{\text{carb}}$  composition of Fortunian-age  
789 global seawater is more faithfully recorded (e.g. Siberia, Morocco, Mongolia), and appears to show  
790 high frequency excursions (including peaks 2p-4p) that record a gradual increase in  $\delta^{13}\text{C}_{\text{carb}}$   
791 towards a large positive excursion (5p) (Figs. 3b-d, 5d-f) (Kouchinsky et al., 2007; Maloof et al.,  
792 2010; Smith et al., 2015). Crucially, however, this interval of high frequency  $\delta^{13}\text{C}_{\text{carb}}$  variability  
793 suffers from a significant dearth of radiometric anchor-points, robust differentiation in SSF  
794 zonation, or differentiation of  $\delta^{13}\text{C}_{\text{carb}}$  peaks of distinct magnitude. Sections of the Anti-Atlas  
795 Mountains in Morocco and along the Sukharikha River of northwest Siberia have been proposed  
796 as continuous reference sections for correlative trends in Fortunian global seawater  $\delta^{13}\text{C}$   
797 (Kouchinsky et al., 2007; Maloof et al., 2010). However, the absolute magnitude and number of  
798 peaks are thought to vary between and within regions (e.g. Smith et al., 2015). At present, the  
799 published section information in both of these areas is insufficiently detailed to accurately  
800 constrain the position of individual exposure surfaces. We note that the Fortunian remains the  
801 interval of greatest uncertainty in our correlation and demands future targeted study, integrating  
802 high resolution chemostratigraphic data with detailed sedimentological, biostratigraphic and  
803 sequence stratigraphic information and, where possible, high resolution radiometric age

804 constraints. Higher resolution  $\delta^{13}\text{C}_{\text{carb}}$  datasets may also permit more statistically significant peak  
805 correlation through use of dynamic programming algorithms, as has been demonstrated for  
806 Atdabanian successions of Morocco (Hay et al., 2019).

### 807 *5.7 The position of the ZHUCE relative to peaks 5p and 6p*

808 Below we consider alternative temporal positions for the ZHUCE and the excursion recorded  
809 in the Salaany Gol Formation. For ease of reference, alternative correlations are incorporated into  
810 Model A relative to models B and C, however their relative positions and uncertainties should be  
811 considered in isolation.

812 The upper Zhujiqing Formation (Dahai Member) of the Yangtze Platform records a prominent  
813 positive  $\delta^{13}\text{C}_{\text{carb}}$  excursion with an onset approximately coincident with the FADs of the mollusks  
814 *Aldanella attleborensis* and *Watsonella crosbyi* (Figs. 8-10, Table S3, Li et al., 2011; Parkhaev  
815 and Karlova, 2011; Steiner et al., 2020). The FAD of *Watsonella crosbyi* occurs prior to the apex  
816 of 5p, or immediately following recovery from 5p in sections of the western Anabar Shield, and  
817 may be approximately contemporaneous in the Bayangol Fm of the Zavkhan Terrane, Mongolia  
818 (Kouchinsky et al., 2017; Smith et al., 2015) (but see section 5.8). Peak 5p is followed by 6p in  
819 Cambrian Stage 2 strata of Siberia and Morocco, but the relative position of the singular excursion  
820 recorded in the Dahai Member has been problematic (Steiner et al., 2020). Possible regional  
821 variability in the magnitude of the ZHUCE in South China, in addition to widespread phosphorite  
822 deposition of the underlying Zhongyicun Member in some areas of the Yangtze Platform,  
823 complicates the utility of  $\delta^{13}\text{C}_{\text{carb}}$  chemostratigraphy for accurately determining the correct  
824 correlation of the peak recorded in the Dahai Member (Steiner et al., 2020).



826 **Fig. 8. High-resolution Cambrian biostratigraphy resulting from models A to C.** Note that  
827 first occurrences are pinned only within sections that have high-resolution  $\delta^{13}\text{C}_{\text{carb}}$  data. As such,  
828 first appearances within siliciclastic-dominated successions remain uncalibrated. The single  
829 specimen of *Aldanotreta* sp. (brachiopod) reported from the upper Zhongyicun Member (Table  
830 S2) may instead represent a tommotiid fragment; however, this cannot be confirmed due to the  
831 poor quality of the specimen.

832

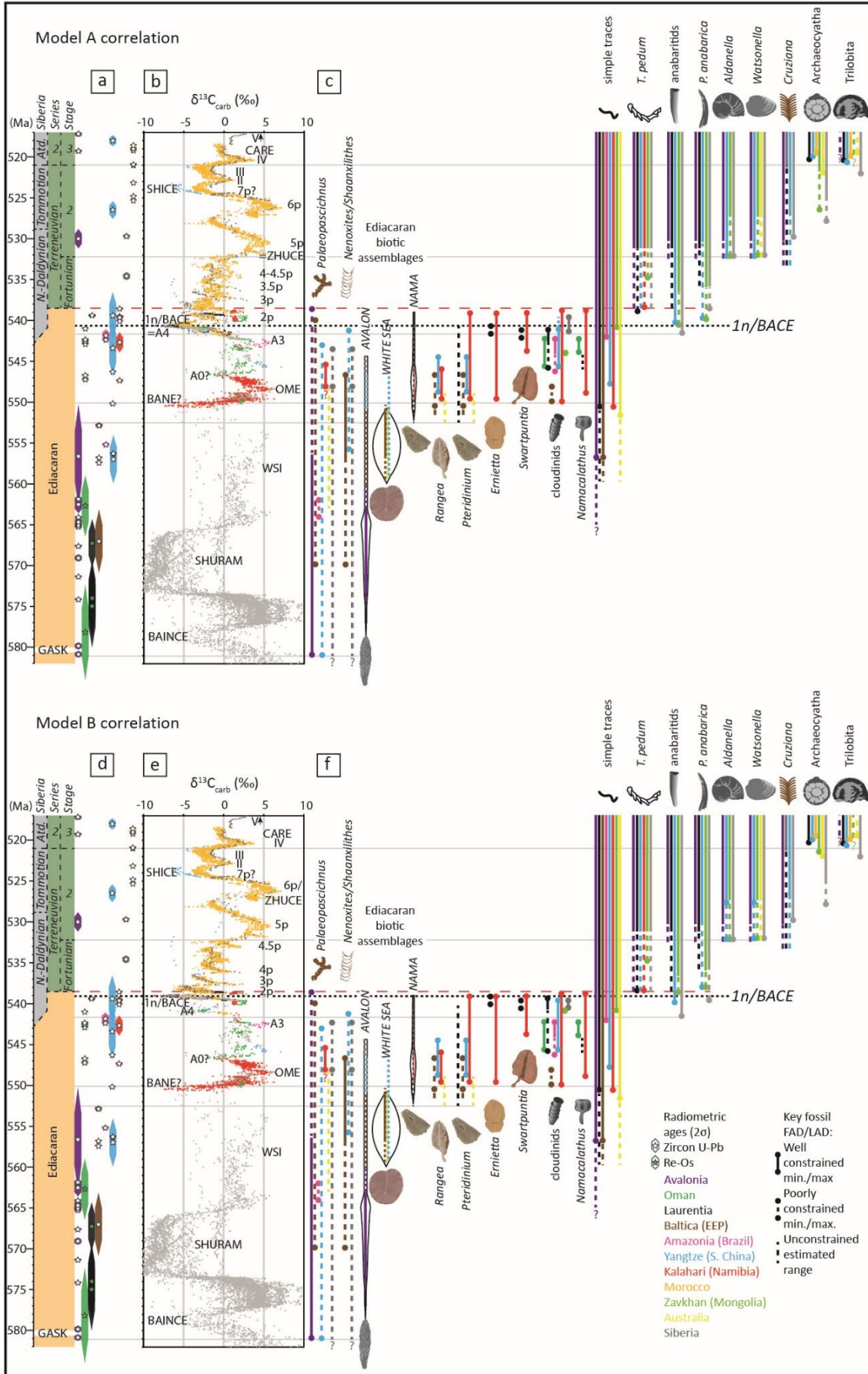
833 Model A (Figs. 3b, 8a, 9b,c) shows the result of correlating the ZHUCE with 5p, which may be  
834 more consistent with a depositional hiatus of longer duration that separates the Dahai Member  
835 from the overlying Shiyantou Formation. In this correlation, the FAD of tommotiids in South  
836 China significantly predates Siberia (Fig. 8a), and maximum  $\delta^{13}\text{C}_{\text{carb}}$  values of the Dahai Member  
837 are greater than 5p in the Siberian and Moroccan profiles. However, Model A results in a relatively  
838 consistent (possibly slightly earlier) FAD of the mollusks *Watsonella* and *Aldanella* relative to  
839 Siberia (Fig. 9c), whereas Model B results in a slightly delayed FAD of these genera in South  
840 China (Figs. 8b and 9f). The correlation of ZHUCE with 5p is also supported by SSF  
841 biostratigraphy of the Yanjiahe Fm, where peak values in Unit 3 occur within the SSF Zone 2  
842 (*Purella antiqua*), which would be consistent with a pre-5p excursion in other localities.

843 In models B and C, the ZHUCE is correlated with peak 6p (Figs. 3c,d, 8b,c, 9f, 10c) and  
844 negative  $\delta^{13}\text{C}_{\text{carb}}$  values associated with phosphatic lithologies of the Zhongyicun Member are not  
845 considered useful for global chemostratigraphic correlation. Correlation of the ZHUCE with 6p  
846 may be justified by the best fit of  $\delta^{13}\text{C}_{\text{carb}}$  data (particularly maximum values at Xiaotan section),  
847 but also by recognition of the more consistent age for the resulting FAD of tommotiids in South

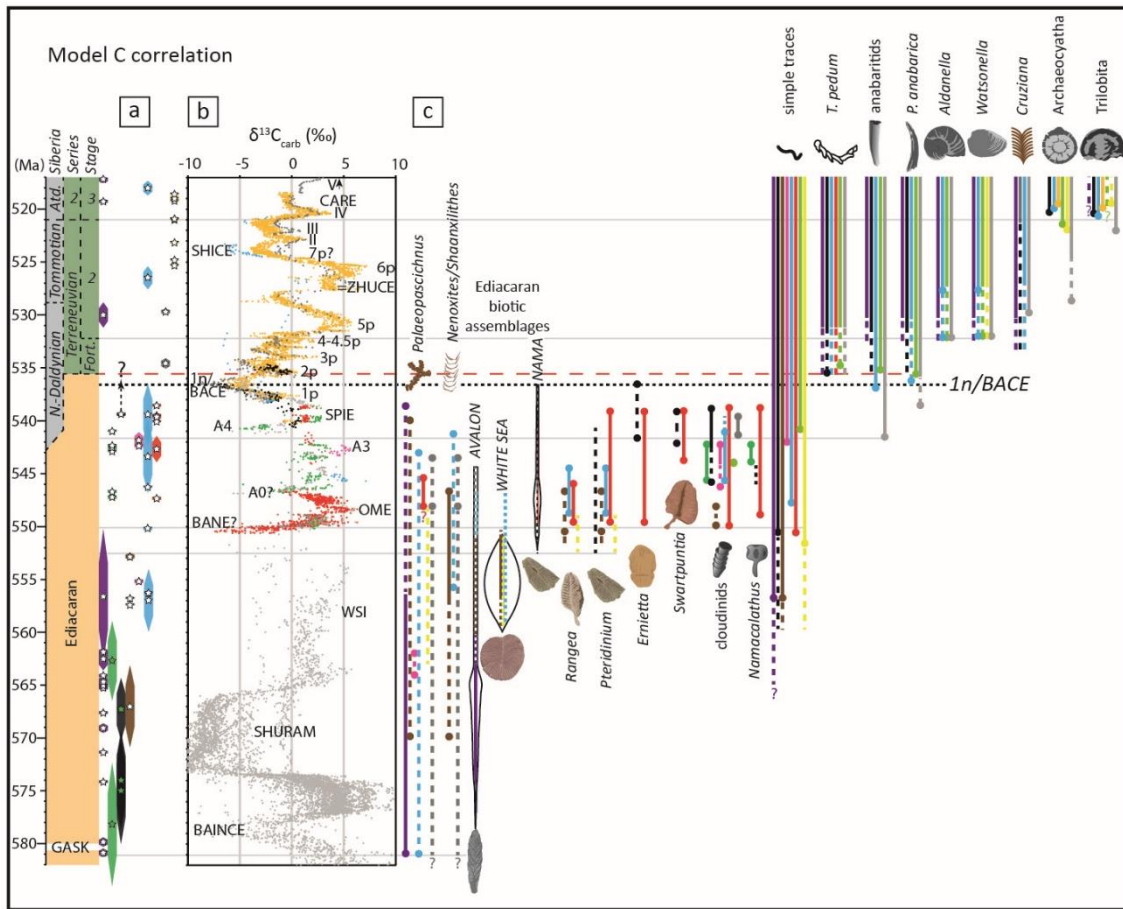
848 China relative to Siberia (Fig. 8b,c). In Model B, positive  $\delta^{13}\text{C}_{\text{carb}}$  in Yanjiahe Unit 3 are correlated  
849 with peak 5p, and peak 6p is absent from this formation in recognition of the depositional hiatus  
850 separating the Yanjiahe Formation from the overlying Shuijingtuo Formation (Steiner et al., 2020).  
851 Robust differentiation between these correlations is currently hampered by a lack of radiometric  
852 data and discontinuous carbonate sections from this interval in South China.

853 *5.8 Correlation of the Salaany Gol Formation (Zavkhan Terrane, Mongolia) with peak 6p vs peak*  
854 *IV*

855 A basal Tommotian (Stage 2) age for the lower Salaany Gol (Salaagol) Formation of SW  
856 Mongolia was justified by Smith et al. (2015) on the basis of an absence of trilobites in this unit,  
857 which in their view makes the excursion equivalent to positive peak 6p of the Siberian scale (shown  
858 in Model A of Figs 3a, 8a, 9b). However, the archaeocyathan assemblage of the lower Salaany Gol  
859 Formation includes approximately 30 distinct species (up to 16 species per single reef; Zhuravlev  
860 and Naimark, 2005), which are widespread throughout Mongolian, Altay-Sayan and  
861 Transbaikalian terranes and occur permanently below the first trilobites in each area (Debrenne et  
862 al., 2015; Dyatlova and Sycheva, 1999; Osadchaya and Kotel'nikov, 1998; Zhuravleva et al.,  
863 1997). In turn, this first trilobite species assemblage is also the same and belongs to the *Resimopsis*  
864 trilobite Zone, which contains species of the middle Atdabanian (Stage 3) *Repinaella* trilobite Zone  
865 of the Siberian Platform and lacks any earlier trilobite elements (Astashkin et al., 1995; Korobov,  
866 1989, 1980). Landing and Kruse (2017) noted these inconsistencies and suggested that the positive  
867  $\delta^{13}\text{C}_{\text{carb}}$  excursion in the lower Salaany Gol Formation is rather an equivalent of the middle  
868 Atdabanian  $\delta^{13}\text{C}_{\text{carb}}$  excursion IV of the Siberian Platform, which fits better to both archaeocyath  
869 and trilobite biostratigraphies. The other suggestion of Smith et al. (2015) concerning the absence



871 **Fig. 9. Biostratigraphic output resulting from Model A (a–c) and Model B (d–f) for the**  
 872 **interval ~551–517 Ma. Includes (a,d) radiometric constraints, (b,e)  $\delta^{13}\text{C}_{\text{carb}}$ , and (c,f) First**  
 873 **Appearance Datum (FAD) and Last Appearance Datum (LAD) of key Ediacaran-Cambrian fossils**  
 874 **(Table S3). Black dotted line marks the temporal position of the 1n/BACE nadir. Red dashed line**  
 875 **marks the Ediacaran-Cambrian boundary as defined by the maximum age for the first appearance**  
 876 **datum of *Treptichnus pedum*. Note that uncertainty remains in ichnofossil assignment of the traces**  
 877 **in the Mistaken Point Formation of Avalonia (Warren et al., 2020).**



878

879 **Fig. 10. Biostratigraphic output resulting from Model C (a–c) for the interval ~551–517 Ma.**  
 880 **Includes (a) radiometric constraints, (b)  $\delta^{13}\text{C}_{\text{carb}}$ , and (c) First Appearance Datum (FAD) and Last**  
 881 **Appearance Datum (LAD) of key Ediacaran-Cambrian fossils (Table S3). Black dotted line marks**



882 the temporal position of the 1n/BACE nadir. Red dashed line marks the Ediacaran-Cambrian  
883 boundary as defined by the maximum age for the first appearance datum of *Treptichnus pedum*. In  
884 this figure, the FAD of *T. pedum* is interpreted to post-date the BACE nadir in all regions (max.  
885 FAD in upper Esmeralda Mb, Nevada, Fig. 5c), and the age of the lower Nomtsas Fm at  
886 Swartkloofberg section does not anchor the FAD of *T. pedum* in Namibia (see discussion in Section  
887 4). Key provided in Fig. 9.

888  
889 of upper Atdabanian and Botoman (stages 3 and 4) faunal elements from the Salaany Gol  
890 Formation is correct and supported by the restudy of archaeocyath species assemblage, which is  
891 the same through the entire formation (Cordie et al., 2019; Debrenne et al., 2015; Zhuravlev, 1998).

892 We agree with Smith et al. (2015) that the magnitude of the positive  $\delta^{13}\text{C}_{\text{carb}}$  excursion reported  
893 from the Salaany Gol Formation fits well with peak 6p on the reference scale, but greatly exceeds  
894 the magnitude of peak IV (Figs. 3, 5f, Table S2). However, we also note that the regional  $\delta^{13}\text{C}_{\text{carb}}$   
895 record from the Zavkhan terrane throughout the underlying Zuun-Arts and Bayangol formations  
896 frequently exhibits more extreme values (positive and negative) relative to other late Ediacaran  
897 and lower Cambrian records from Siberia, Morocco and elsewhere. Models B and C (Figs. 3c,d,  
898 8b,c, 9e,f, 10b,c) reposition the Salaany Gol Formation to the Atdabanian, with the uppermost  
899 Bayan Gol Formation occupying a position relative to peak 6p, and implies poor expression of  
900 peak 5p, possibly within lower Member BG5 of Smith et al. (2015) (Fig. 5f). We stress, however,  
901 that peak correlation throughout the Fortunian and Stage 2 of Mongolia, and globally, remains  
902 poorly constrained.

903 5.9 Age and correlation of Terreneuvian – Series 2 strata of Australia

904 The Arrowie and Stansbury basins contain a rich assemblage of lower Cambrian fossils,  
905 including the regional first appearance of archaeocyaths, trilobites, bradoriids and tommotiids.  
906 Betts et al. (2019, 2018, 2017a, 2017b, 2016) and Jago et al. (2020) refined the lower Cambrian  
907 biostratigraphy for South Australia developed by Daily (1990, 1972), Laurie (1986), Gravestock  
908 (1984), Bengtson et al. (1990), Zhuravlev and Gravestock (1994), and Gravestock et al. (2001)  
909 and added  $\delta^{13}\text{C}_{\text{carb}}$  chemostratigraphy. Contrary to previous workers, Betts et al. (2019, 2018,  
910 2017a, 2017b, 2016) and Jago et al. (2020) suggested that lower units of fossiliferous strata of the  
911 Arrowie and Stansbury basins be repositioned to stages 2 and 3 instead of stages 3 and 4,  
912 respectively. These justifications were mostly based on tommotiid biostratigraphy, with little  
913 reference to other biostratigraphic constraints. However, Australian tommotiids are highly  
914 endemic species and some genera are unknown even beyond the Australian-Antarctic faunal  
915 province of Gondwana, while other faunal elements, including archaeocyaths, trilobites,  
916 bradoriids, mollusks and brachiopods are much more widespread, although at the generic level  
917 (Bengtson et al., 1990; Betts et al., 2017b; Brock et al., 2000; Gravestock et al., 2001; Laurie,  
918 1986). In dismissing the biostratigraphic value of archaeocyaths, for instance, these authors arrive  
919 at a correlation of their *Kulparina rostrata* tommotiid Zone and the regionally pre-trilobitic portion  
920 of their succeeding *Micrina etheridgei* Zone with the Cambrian Stage 2, even though these zones  
921 collectively coincide with the *Warriootacyathus wilkawillinensis*, *Spirillicyathus tenuis* and  
922 *Jugalicyathus tardus* archaeocyath zones (Zhuravlev and Gravestock, 1994), dated as Atdabanian  
923 in Siberian terms (Stage 3). Likewise, comparison of archaeocyath genera in common with South  
924 China indicates a correlation with trilobite-bearing upper Qiongzhusian-lower Canglangpuan  
925 (Stage 3) strata in that region (A. Yang et al., 2016). The same conclusions contradicting the

926 correlations of Betts et al. (2018, 2017a) follow from analysis of the biostratigraphic distribution  
927 of any other fossil group present in these tommotiid-based zones, including bradoriids,  
928 brachiopods (Kruse et al., 2017) and mollusks (Parkhaev, 2019). In general, tommotiids and coeval  
929 early small shelly fossils in South Australia are not indicative of the Terreneuvian because  
930 representatives of all other co-occurring fossil groups (archaeocyaths, bradoriids, brachiopods,  
931 mollusks) are restricted to post-Terreneuvian strata in Siberia, South China, Laurentia and other  
932 regions, and more precisely to global stages 3 and 4 (Kruse et al., 2017; Parkhaev, 2019), which  
933 suggests different, younger ages for some of the  $\delta^{13}\text{C}_{\text{carb}}$  peaks, rather than those accepted by Betts  
934 et al. (2018). In our correlation, we have repositioned some of these Australian  $\delta^{13}\text{C}_{\text{carb}}$  data to  
935 maintain consistency with both the regional stratigraphic correlation of Betts et al. (2018) and  
936 biostratigraphic constraints that are more globally applicable (Figs. 9 and 10, Table S2).

937

## 938 **6. Implications for macroevolutionary dynamics**

939 Our revised correlations have important implications both for the late Ediacaran global  $\delta^{13}\text{C}_{\text{carb}}$   
940 profile and for macroevolutionary dynamics across the BACE interval. Combining the temporal  
941 and spatial distribution of major Ediacaran-Cambrian shelly and trace fossils into these new global  
942  $\delta^{13}\text{C}_{\text{carb}}$ ,  $^{87}\text{Sr}/^{86}\text{Sr}$  and geochronological records, together with older Ediacaran radiometric dates,  
943 allows us to establish temporal and spatial paleobiogeographic trends that significantly diverge  
944 from the accepted consensus (Figs. 8-11; Table S3). These trends are robust despite remaining  
945 uncertainties, and crucially, all age models show the same macroevolutionary trends across the  
946 Ediacaran-Cambrian boundary interval (Figs. 8-10). Namely, that multiple negative  
947  $\delta^{13}\text{C}_{\text{carb}}$  excursions are present in the late Ediacaran record, which do not clearly correlate with

948 extinction events and that SSFs of the *A. trisulcatus* – *P. anabarica* Zone appeared below the  
949 BACE.

950 The available radiometric age constraints for the interval of ~580–538 Ma confirm the temporal  
951 overlap of elements of the Avalon, White Sea and Nama assemblages of the Ediacaran biota, rather  
952 than forming discrete successive assemblages, with the White Sea assemblage being entirely  
953 transitional (Grazhdankin, 2014; Yang et al., 2021). Consistent with previous models, the  
954 Ediacaran biota show a marked decline in diversity ~550, and again ~545 Ma (Boag et al., 2016;  
955 Grazhdankin, 2014; Muscente et al., 2019). Elements of the Avalon and White Sea assemblages  
956 inhabited different basins contemporaneously in the White Sea and Podolia regions of Baltica, and  
957 Australia, until ~552 Ma (Gehling and Droser, 2013; Grazhdankin, 2014), although the age range  
958 of fossiliferous strata of the Ediacara Member remains poorly constrained. Both the Avalon and  
959 White Sea assemblages largely disappeared by ~550 Ma, however some elements of the Avalon  
960 assemblage (e.g. *Charniodiscus*) and White Sea assemblage (e.g. possible *Dickinsonia* sp.) were  
961 likely present until as late as ~545.5 Ma in South China and possibly northern Siberia (e.g. Xiao  
962 et al., 2020). After this time, taxa of the Nama assemblage remained present in the Nama Basin,  
963 Namibia, the Erga Formation of the White Sea region, the Shibantan Member of the Yangtze  
964 Block, South China, and the Wood Canyon Formation of Laurentia. Successions of Armorica  
965 (Spain) and SW Gondwana (Brazil and Paraguay) also host skeletal assemblages of *Cloudina*,  
966 *Namacalathus* and *Corumbella* (Adôrno et al., 2017; Cortijo et al., 2010; Warren et al., 2011),  
967 however these successions remain poorly constrained in time <550 Ma due to a dearth of high  
968 resolution  $\delta^{13}\text{C}_{\text{carb}}$  data. Fossils of the *Palaeopascichnus* group may have extended below ~560  
969 Ma in the Shuram-Wonoka negative excursion interval in South Australia. However, these taxa  
970 are known from ~547–545 Ma in Siberia (Aim Formation), South China (Gaojiashan and

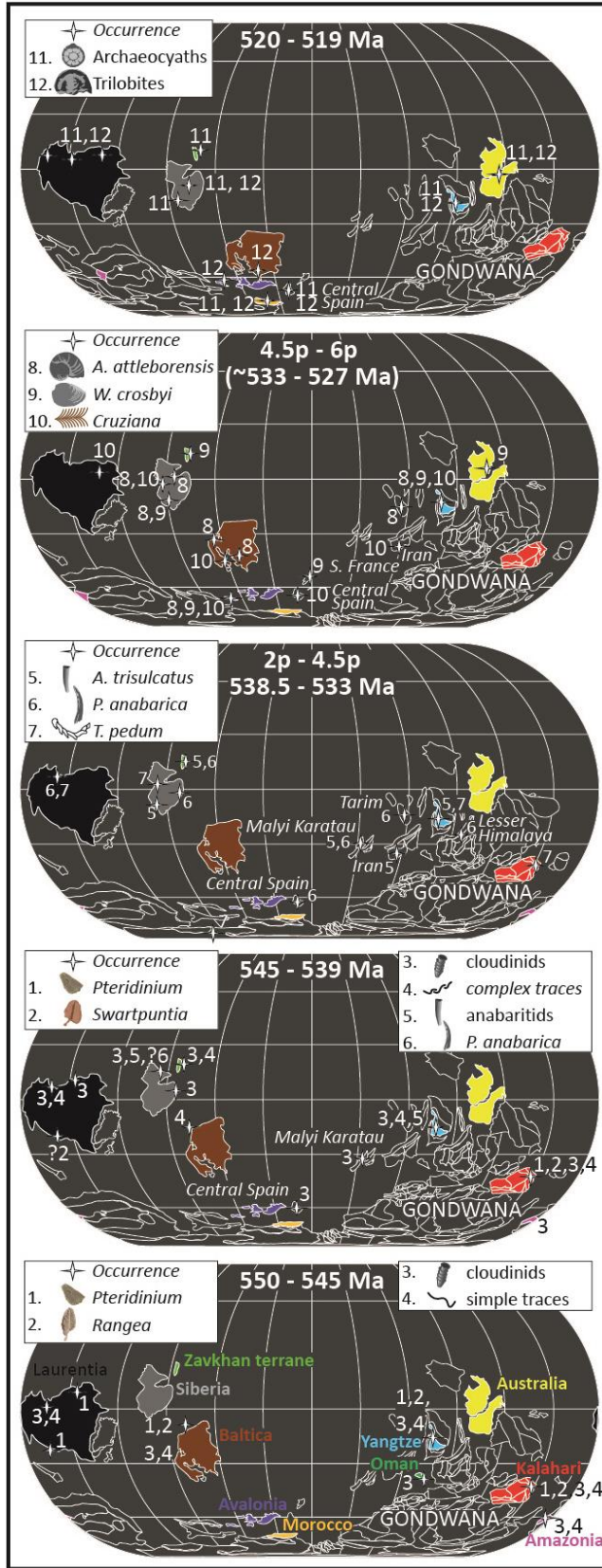


**Fig. 11. Global paleobiogeography at intervals between ~551 and 517 Ma consistent with all age models with paleogeography after (Merdith et al., 2021). Note that the positions of the Zavkhan terrane of Mongolia (bright green), Malyi Karatau of Kazakhstan, and Avalonian microcontinent in this interval remain uncertain (e.g. Landing et al., 2020). Craton coloring is consistent with stratigraphic and biostratigraphic ranges in Figs. 3-5, and 7-10.**

990 Shibantan members, and Liuchapo Formation) and Namibia (Schwarzrand Subgroup), and may  
991 show their greatest range in eastern Newfoundland, where they are found below a Gaskiers age  
992 diamictite (>580 Ma) and even co-occur with *T. pedum* above the basal Cambrian GSSP (Table  
993 S3).

994 Treptichnid trace fossils pre-date the inferred nadir of the BACE in Namibia, and Cambrian-  
995 type shelly fossils of the *Anabarites trisulcatus* – *Protohertzina anabarica* Zone predate the nadir  
996 of the BACE in Siberia and predate or co-occur with the nadir of the BACE in South China (Cai  
997 et al., 2019; Jensen et al., 2000; Zhu et al., 2017). Diverse and complex ichnofossils also predate  
998 the *T. pedum* FAD in a number of sections (e.g. Chen et al., 2019; Gozalo et al., 2003; Jensen et  
999 al., 2000; Zhu et al., 2017). At least three soft-bodied genera of the Nama assemblage are present  
1000 in the Nama Basin, Namibia, post-dating (Model A), coeval with (Model B), or pre-dating (Model  
1001 C) the inferred position of the BACE, and both *Cloudina* and *Namacalathus* occur above the  
1002 inferred recovery from the A4 anomaly in the same section in all models (Fig. 2, Darroch et al.,  
1003 2015; Narbonne et al., 1997; Wood et al., 2015). There are currently no environments that show  
1004 unequivocal co-occurrence of the Cambrian ichnospecies *T. pedum* and Ediacaran skeletal fossils  
1005 *Cloudina* or *Namacalathus*. These taxa, as well as *Nenoxites* (= *Shaanxilithes* in South China)  
1006 became extinct at or before the Ediacaran-Cambrian boundary, as defined by the FAD of *T. pedum*,  
1007 but significantly these extinctions were regional, rather than global events (e.g. *Cloudina* LAD  
1008 may be as early as ~542.3 Ma in Oman (Bowring et al., 2007), but occurred after ~539.6 Ma in  
1009 Namibia (Linnemann et al., 2019)).

1010 Model C may support a range extension for erniettomorphs in *Laurentia* associated with the  
1011 BACE nadir, to an age that is within the lower Cambrian as presently defined (Figs. 5 and 10).

1012 However, Model C may also imply a younger age for the FAD of *T. pedum* (and hence the  
1013 Ediacaran-Cambrian boundary) if this ichnospecies is restricted to a position above the BACE  
1014 recovery as suggested in multiple regions (Figs. 5 and 10, Table S3). The *T. pedum* FAD may  
1015 show broadly synchronous origination at the boundary above recovery from the BACE, with a  
1016 maximum radiometric age constraint of ~538.8 Ma (Linnemann et al., 2019). However, the first  
1017 appearance of this ichnospecies is delayed in the Zavkhan terrane, and is not well constrained  
1018 within the interval 538.8–532 Ma in Siberia, South China or the lower Cambrian boundary type  
1019 section in Avalonia (Table S3). This pattern may be a consequence of local ecological, taphonomic  
1020 and/or lithological controls.

1021 The FADs of Ediacaran and Cambrian shelly fossils are also highly variable temporally and  
1022 spatially (Figs. 8-10). The *Cloudina* – *Namacalathus* assemblage appeared ~550 Ma in the Nama  
1023 Basin and became globally widespread, but asynchronously, thereafter. *Anabarites trisulcatus* and  
1024 *Protohertzina anabarica* FADs, which are commonly recognized as the index fossils of the basal  
1025 Cambrian strata, are in fact oldest in Siberia, where *Anabarites* co-occurs with *Cloudina* at a level  
1026 below the BACE (Figs. 8-10) (Zhu et al., 2017), followed closely by the appearance of these taxa  
1027 in South China (Cai et al., 2019). Cambrian-type skeletal fossils (halkieriids, chancelloriids,  
1028 hyolithelminthes, hyoliths, archaeocyaths and many others) also appear highly asynchronously in  
1029 different basins (Fig. 8).

1030 By contrast, our compilation suggests that the appearance of *Watsonella* and *Aldanella* at  
1031 ~532–531 Ma may have had a broadly synchronous appearance during the same interval on the  
1032 global  $\delta^{13}\text{C}_{\text{carb}}$  profile, however this remains dependent upon the correlation of the ZHUCE in  
1033 South China (Figs. 8-10). The probability of a trilobite biomineralisation event at ~521–518 Ma

1034 is supported by the stratigraphic and paleogeographic distribution of arthropod scratch marks (e.g.  
1035 *Rusophycus*, *Cruziana* and *Diplichnites*), which occur from ~531–525 Ma and pre-date the  
1036 appearance of trilobites and other arthropods in almost every basin by several million years  
1037 (Landing et al., 2020; Paterson et al., 2019). This biomineralisation event may have been driven  
1038 by changing seawater chemistry (e.g. Mg/Ca ratios,  $p\text{CO}_2$ ), causing a shift from aragonite to calcite  
1039 seas (Porter, 2007).

1040 These observations may imply two patterns of first appearance. In the first case, an animal or a  
1041 group of animals appeared first in a single area and became globally widespread much later (e.g.  
1042 Namibian shelly fossils including *Cloudina* and *Namacalathus*, Siberian archaeocyaths). The  
1043 appearance of such organisms probably reflects local conditions most advantageous for their  
1044 oxygen, calcium and other essential requirements. The second type of FADs embraces a broadly  
1045 synchronous global appearance of the same group in remote regions (e.g. mollusks, trilobites).  
1046 Such events can be attributed to global changes of environmental factors (e.g.  $p\text{CO}_2$ , Mg:Ca ion  
1047 ratio) facilitating almost simultaneous biomineralisation of hitherto soft-bodied representatives of  
1048 these groups in different basins, as noted in trilobites (Paterson et al., 2019).

1049 We conclude that the Cambrian Explosion was in fact a protracted Ediacaran-Cambrian  
1050 radiation. All models reveal widespread and correlatable late Ediacaran negative and positive  
1051  $\delta^{13}\text{C}_{\text{carb}}$  excursions between ~550 Ma and the onset of the BACE. In contrast to previous studies  
1052 (Amthor et al., 2003), our correlation demonstrates no significant extinction or faunal turnover  
1053 coincident with the A4 anomaly, or any older negative carbon  $\delta^{13}\text{C}_{\text{carb}}$  perturbation between 550  
1054 Ma and 540 Ma, but rather a series of successive, often regional, originations and minor  
1055 extinctions. The canonical model (Model A) also implies that the disappearance of the Nama



1056 assemblage post-dated the BACE, whereas Model C may be compatible with a coincident  
1057 disappearance of this assemblage with the BACE nadir. Regardless, the pre-BACE appearance of  
1058 anabaritids and treptichnid traces in all models also argues against a mass extinction event  
1059 coincident with the BACE.

1060 While the near synchronous global appearance of trilobites may support a calcification  
1061 (biomineralisation) event in this group (Landing et al., 2020; Paterson et al., 2019), the radiation  
1062 of other skeletal biota was generally highly asynchronous, with varying tempos in different basins  
1063 (Figs. 8-11). This may reflect both a diversity gradient formed by clade origination in low  
1064 latitudinal basins (Siberia, Mongolia, Chinese and Namibian Gondwana) and then migration to  
1065 higher latitudes (e.g. Avalonia, Morocco) (Fig. 11, e.g. Jablonski et al., 2006, but see Landing et  
1066 al., 2020), and also a highly heterogeneous local landscape of redox and/or nutrient regimes. The  
1067 origination of many skeletal groups, including cloudinids, mollusks and trilobites, as well as the  
1068 Ediacaran-Cambrian boundary itself, all seem to coincide with the succession of marked positive  
1069  $\delta^{13}\text{C}_{\text{carb}}$  excursions (Figs. 9 and 10). Peak  $\delta^{13}\text{C}_{\text{carb}}$  values during positive excursions during  
1070 Cambrian stages 2–4 on the Siberian Platform have been proposed to record pulses of nutrients  
1071 and oxygen into shallow marine seas that promoted biodiversification (He et al., 2019). By  
1072 contrast, global  $\delta^{13}\text{C}_{\text{carb}}$  excursions of regionally variable magnitude, from the level of the BACE  
1073 to 6p, may reflect a combination of changes in glacioeustatic sea level overprinted by regional  
1074 palaeomarine redox and nutrient heterogeneity. The age model framework constructed herein  
1075 provides a comprehensive and editable template by which the operation of these, and other driving  
1076 forces, in shaping the Ediacaran-Cambrian radiation of early animals may be explored.

1077

1078 **Acknowledgments**

1079 **Funding:** FB, RW, GS, SWP, YZ and MZ acknowledge funding from the joint NERC-NSFC  
1080 Biosphere Evolution Transitions and Resilience (BETR) programme (NE/P013643/1,  
1081 NSFC/41661134048), MZ from the Strategic Priority Research Program (B) of the Chinese  
1082 Academy of Sciences (XDB18000000, XDB 26000000), FB, SWP and GS from NERC project  
1083 NE/R010129/1, and RW, SWP and FB from NERC Project NE/T008458/1. SWP acknowledges  
1084 support from a Royal Society Wolfson Research Merit Award. AZ from Scientific Project 04-1-  
1085 21 of the State Order of the Government of the Russian Federation to the Lomonosov Moscow  
1086 State University (No. 121031600198-2). We thank C. Chilcott for technical support. We are  
1087 grateful to H. Mocke and C. Hoffmann of the Geological Survey of Namibia and the Ministry of  
1088 Mines and Energy, Namibia. We thank B. Romer and L. Gessert for access to Farm Swartpunt.  
1089 We thank Irene Gomez Perez for enlightening discussion regarding Ara Group stratigraphy. We  
1090 thank Lucas Warren and one anonymous reviewer for constructive comments and suggestions that  
1091 improved the paper. **Author contributions:** FB conceived the project, FB compiled all data with  
1092 the help of AZ, GS, RW, CY and MZ. FB constructed the age model with insight from all authors.  
1093 FB, AC, and RW collected and analyzed Namibian samples. All authors contributed to writing the  
1094 paper. **Competing interests:** Authors declare no competing interests; **Data and materials**  
1095 **availability:** All data, including expanded geological information and full age models are available  
1096 in the Supplementary Information.

1097

1098

1099

1100

1101 **References**

- 1102 Adôrno, R.R., do Carmo, D.A., Germs, G., Walde, D.H.G., Denezine, M., Boggiani, P.C., Sousa  
1103 e Silva, S.C., Vasconcelos, J.R., Tobias, T.C., Guimarães, E.M., Vieira, L.C., Figueiredo,  
1104 M.F., Moraes, R., Caminha, S.A., Suarez, P.A.Z., Rodrigues, C. V., Caixeta, G.M., Pinho,  
1105 D., Schneider, G., Muyambag, R., 2017. *Cloudina luciano* (Beurlen and Sommer, 1957),  
1106 Tamengo Formation, Ediacaran, Brazil: Taxonomy, analysis of stratigraphic distribution  
1107 and biostratigraphy. *Precambrian Res.* 301, 19–35.
- 1108 Ahm, A.-S.C., Bjerrum, C.J., Hoffman, P.F., Macdonald, F.A., Maloof, A.C., Rose, C. V.,  
1109 Strauss, J. V., Higgins, J.A., 2021. The Ca and Mg isotope record of the Cryogenian  
1110 Trezona carbon isotope excursion. *Earth Planet. Sci. Lett.* 568, 117002.
- 1111 Amthor, J.E., Grotzinger, J.P., Schröder, S., Bowring, S.A., Ramezani, J., Martin, M.W., Matter,  
1112 A., 2003. Extinction of *Cloudina* and *Namacalathus* at the Precambrian-Cambrian boundary  
1113 in Oman. *Geology* 31, 431–434.
- 1114 An, Z., Jiang, G., Tong, J., Tian, L., Ye, Q., Song, Huyue, Song, Haijun, 2015. Stratigraphic  
1115 position of the Ediacaran Miaohu biota and its constrains on the age of the upper  
1116 Doushantuo  $\delta^{13}\text{C}$  anomaly in the Yangtze Gorges area, South China. *Precambrian Res.* 271,  
1117 243–253. <https://doi.org/10.1016/j.precamres.2015.10.007>
- 1118 Astashkin, V.A., Pegel, T. V., Repina, L.N., Rozanov, A.Y., Shabanov, Y.Y., Zhuravlev, A.Y.,  
1119 Sukhov, S.S., Sundukov, V.M., 1995. The Cambrian System of the foldbelts of Russia and  
1120 Mongolia. Correlation chart and explanatory notes. *Int. Union Geol. Sci. Publ.* 32, 1–132.
- 1121 Babcock, L.E., Peng, S., Zhu, M., Xiao, S., Ahlberg, P., 2014. Proposed reassessment of the  
1122 Cambrian GSSP. *J. African Earth Sci.* 98, 3–10.
- 1123 Bengtson, S., Conway Morris, S., Cooper, B.J., Jell, P.A., Runnegar, B.N., 1990. Early Cambrian  
1124 fossils from South Australia. *Mem. Assoc. Australas. Palaeontols.* 9, 1–364.
- 1125 Betts, M.J., Claybourn, T.M., Brock, G.A., Jago, J.B., Skovsted, C.B., Paterson, J.R., 2019.  
1126 Shelly fossils from the lower Cambrian White Point Conglomerate, Kangaroo Island, South  
1127 Australia. *Acta Palaeontol. Pol.* 64, 489–522.
- 1128 Betts, M.J., Paterson, J., Jago, J., Jacquet, S., Skovsted, C., Topper, T., Brock, G., 2017a. A new  
1129 lower Cambrian shelly fossil biostratigraphy for South Australia, Reply. *Gondwana Res.* 44,  
1130 262–264.
- 1131 Betts, M.J., Paterson, J.R., Jacquet, S.M., Andrew, A.S., Hall, P.A., Jago, J.B., Jagodzinski, E.A.,  
1132 Preiss, W. V., Crowley, J.L., Brougham, T., Mathewson, C.P., García-Bellido, D.C.,  
1133 Topper, T.P., Skovsted, C.B., Brock, G.A., 2018. Early Cambrian chronostratigraphy and  
1134 geochronology of South Australia. *Earth-Science Rev.* 185, 498–543.
- 1135 Betts, M.J., Paterson, J.R., Jago, J.B., Jacquet, S.M., Skovsted, C.B., Topper, T.P., Brock, G.A.,  
1136 2017b. Global correlation for the early Cambrian of South Australia: Shelly fauna of the  
1137 *Dailyatia odyssei* Zone. *Gondwana Res.* 46, 240–279.
- 1138 Betts, M.J., Paterson, J.R., Jago, J.B., Jacquet, S.M., Skovsted, C.B., Topper, T.P., Brock, G.A.,  
1139 2016. A new lower Cambrian shelly fossil biostratigraphy for South Australia. *Gondwana*  
1140 *Res.* 36, 176–208.
- 1141 Boag, T.H., Darroch, S.A.F., Laflamme, M., 2016. Ediacaran distributions in space and time:  
1142 testing assemblage concepts of earliest macroscopic body fossils. *Paleobiology* 42, 574–  
1143 594.
- 1144 Bold, U., Crüger Ahm, A.S., Schrag, D.P., Higgins, J.A., Jamsran, E., Macdonald, F.A., 2020.  
1145 Effect of dolomitization on isotopic records from Neoproterozoic carbonates in  
1146 southwestern Mongolia. *Precambrian Res.* 350, 105902.

1147 Bowring, S.A., Grotzinger, J.P., Condon, D.J., Ramezani, J., Newall, M.J., Allen, P.A., 2007.  
1148 Geochronologic constraints on the chronostratigraphic framework of the Neoproterozoic  
1149 Huqf Supergroup, Sultanate of Oman. *Am. J. Sci.* 307, 1097–1145.

1150 Bowring, S.A., Grotzinger, J.P., Isachsen, C.E., Knoll, A.H., Pelechaty, S.M., Kolosov, P., 1993.  
1151 Calibrating rates of Early Cambrian evolution. *Science*. 261, 1293–1298.

1152 Brasier, M., Cowie, J., Taylor, M., 1994. Decision on the Precambrian-Cambrian boundary  
1153 stratotype. *Episodes* 17, 3–8.

1154 Brasier, M.D., Magaritz, M., Corfield, R., Luo, H., Wu, X., Ouyang, L., Jiang, Z., Hamdi, B.,  
1155 He, T., Fraser, A.G., 1990. The carbon- and oxygen-isotope record of the Precambrian-  
1156 Cambrian boundary interval in China and Iran and their correlation. *Geol. Mag.* 127, 319–  
1157 332.

1158 Brasier, M.D., Rozanov, A.Y., Zhuravlev, A.Y., Corfield, R.M., Derry, L.A., 1994. A carbon  
1159 isotope reference scale for the Lower Cambrian Series in Siberia (Report of IGCP Project  
1160 303). *Geol. Mag.* 131, 767–783.

1161 Brasier, M.D., Shields, G., Kuleshov, V.N., Zhegallo, E.A., 1996. Integrated chemo- and  
1162 biostratigraphic calibration of early animal evolution: Neoproterozoic-early Cambrian of  
1163 southwest Mongolia. *Geol. Mag.* 133, 445–485.

1164 Brock, G.A., Engelbretsen, M.J., Jago, J.B., Kruse, P.D., Laurie, J.R., Shergold, J.H., Shi, G.R.,  
1165 Sorauf, J.E., 2000. Palaeobiogeographic affinities of Australian Cambrian faunas. *Mem.*  
1166 *Assoc. Australas. Palaeontols.* 23, 1–61.

1167 Bykova, N., LoDuca, S.T., Ye, Q., Marusin, V., Grazhdankin, D., Xiao, S., 2020. Seaweeds  
1168 through time: Morphological and ecological analysis of Proterozoic and early Paleozoic  
1169 benthic macroalgae. *Precambrian Res.* 350, 105875.

1170 Cai, Y., Xiao, S., Li, G., Hua, H., 2019. Diverse biomineralizing animals in the terminal  
1171 Ediacaran Period herald the Cambrian explosion. *Geology* 47, 380–384.  
1172 <https://doi.org/10.1130/G45949.1>

1173 Chen, Z., Zhou, C., Xiao, S., Wang, W., Guan, C., Hua, H., Yuan, X., 2014. New Ediacaran  
1174 fossils preserved in marine limestone and their ecological implications. *Sci. Rep.* 4, 4180.

1175 Chen, Z., Zhou, C., Yuan, X., Xiao, S., 2019. Death march of a segmented and trilobate  
1176 bilaterian elucidates early animal evolution. *Nature* 573, 412–415.  
1177 <https://doi.org/10.1038/s41586-019-1522-7>

1178 Condon, D., Zhu, M., Bowring, S., Wang, W., Yang, A., Jin, Y., 2005. U-Pb ages from the  
1179 neoproterozoic Doushantuo Formation, China. *Science*. 308, 95–98.  
1180 <https://doi.org/10.1126/science.1107765>

1181 Cordie, D.R., Dornbos, S.Q., Marenco, P.J., Oji, T., Gonchigdorj, S., 2019. Depauperate  
1182 skeletonized reef-dwelling fauna of the early Cambrian: insights from archaeocyathan reef  
1183 ecosystems of western Mongolia. *Palaeogeogr. Palaeoclimatol. Palaeoecol.* 514, 206–221.

1184 Cortijo, I., Martí Mus, M., Jensen, S., Palacios, T., 2010. A new species of *Cloudina* from the  
1185 terminal Ediacaran of Spain. *Precambrian Res.* 176, 1–10.

1186 Cui, H., Grazhdankin, D.V., Xiao, S., Peek, S., Rogov, V.I., Bykova, N.V., Sievers, N.E., Liu,  
1187 X.M., Kaufman, A.J., 2016a. Redox-dependent distribution of early macro-organisms:  
1188 Evidence from the terminal Ediacaran Khatyspyt Formation in Arctic Siberia. *Palaeogeogr.*  
1189 *Palaeoclimatol. Palaeoecol.* 461, 122–139. <https://doi.org/10.1016/j.palaeo.2016.08.015>

1190 Cui, H., Kaufman, A.J., Xiao, S., Peek, S., Cao, H., Min, X., Cai, Y., Siegel, Z., Liu, X.M., Peng,  
1191 Y., Schiffbauer, J.D., Martin, A.J., 2016b. Environmental context for the terminal Ediacaran  
1192 biomineralization of animals. *Geobiology* 14, 344–363. <https://doi.org/10.1111/gbi.12178>

- 1193 Cui, H., Kaufman, A.J., Zou, H., Kattan, F.H., Trusler, P., Smith, J., Ivantsov, A.Y., Rich, T.H.,  
1194 Al Qubani, A., Yazedi, A., Lui, X.M., 2020a. Primary or secondary? A dichotomy of the  
1195 strontium isotope anomalies in the Ediacaran carbonates of Saudi Arabia. *Precambrian Res.*  
1196 105720.
- 1197 Cui, H., Warren, L. V., Uhlein, G.J., Okubo, J., Liu, X.M., Plummer, R.E., Baele, J., Goderis, S.,  
1198 Claeys, P., Li, F., 2020b. Global or regional? Constraining the origins of the middle Bambuí  
1199 carbon cycle anomaly in Brazil. *Precambrian Res.* 348, 105861.
- 1200 Cui, H., Xiao, S., Cai, Y., Peek, S., Plummer, R.E., Kaufman, A.J., 2019. Sedimentology and  
1201 chemostratigraphy of the terminal Ediacaran Dengying Formation at the Gaojiashan section,  
1202 South China. *Geol. Mag.* 156, 1924–1948.
- 1203 Daily, B., 1990. Cambrian stratigraphy of Yorke Peninsula. *Geol. Soc. Aust. Spec. Publ.* 16,  
1204 215–229.
- 1205 Daily, B., 1972. The base of the Cambrian and the first Cambrian faunas, in: Jones, J.B.,  
1206 McGowran, B. (Eds.), *Stratigraphic Problems of the Late Precambrian and Early Cambrian.*  
1207 University of Adelaide Centre for Precambrian Research Special Paper, pp. 13–42.
- 1208 Darroch, S.A.F., Cribb, A.T., Buatois, L.A., Germs, G.J.B., Kenchington, C.G., Smith, E.F.,  
1209 Mocke, H., O’Neil, G.R., Schiffbauer, J.D., Maloney, K.M., Racicot, R.A., Turk, K.A.,  
1210 Gibson, B.M., Almond, J., Koester, B., Boag, T.H., Tweedt, S.M., Laflamme, M., 2021.  
1211 The trace fossil record of the Nama Group, Namibia: Exploring the terminal Ediacaran roots  
1212 of the Cambrian explosion. *Earth-Science Rev.* 212, 103435.
- 1213 Darroch, S.A.F., Smith, E.F., Laflamme, M., Erwin, D.H., 2018. Ediacaran Extinction and  
1214 Cambrian Explosion. *Trends Ecol. Evol.* 33, 653–663.  
1215 <https://doi.org/10.1016/j.tree.2018.06.003>
- 1216 Darroch, S.A.F., Sperling, E.A., Boag, T.H., Racicot, R.A., Mason, S.J., Morgan, A.S., Tweedt,  
1217 S., Myrow, P., Johnston, D.T., Erwin, D.H., Laflamme, M., 2015. Biotic replacement and  
1218 mass extinction of the Ediacara biota. *Proc. R. Soc. B Biol. Sci.* 282, 20151003.
- 1219 Debrenne, F., Zhuravlev, A.Y., Kruse, P.D., 2015. General features of the Archaeocyatha.  
1220 Systematic descriptions: Archaeocyatha, in: *Treatise on Invertebrate Paleontology, Pt. E*  
1221 *Porifera Revised (Hypercalcified Porifera).* Univ. Kansas Paleontol. Inst., Lawrence, KA,  
1222 pp. 845–1084.
- 1223 Dilliard, K.A., Pope, M.C., Coniglio, M., Hasiotis, S.T., Lieberman, B.S., 2007. Stable isotope  
1224 geochemistry of the lower Cambrian Sekwi Formation, Northwest Territories, Canada:  
1225 Implications for ocean chemistry and secular curve generation. *Palaeogeogr.*  
1226 *Palaeoclimatol. Palaeoecol.* 256, 174–194. <https://doi.org/10.1016/j.palaeo.2007.02.031>
- 1227 Duda, J.P., Zhu, M., Reitner, J., 2016. Depositional dynamics of a bituminous carbonate facies in  
1228 a tectonically induced intra-platform basin: the Shibantan Member (Dengying Formation,  
1229 Ediacaran Period). *Carbonates and Evaporites* 31, 87–99. [https://doi.org/10.1007/s13146-](https://doi.org/10.1007/s13146-015-0243-8)  
1230 [015-0243-8](https://doi.org/10.1007/s13146-015-0243-8)
- 1231 Dyatlova, I.N., Sycheva, R.F., 1999. New data on Lower Cambrian biostratigraphy of Eastern  
1232 Sayan. *Stratigr. Geol. Korrelyatsiya* 7, 3–13.
- 1233 Gehling, J., Droser, M.L., 2013. How well do fossil assemblages of the Ediacara Biota tell time?  
1234 *Geology* 41, 447–450.
- 1235 Germs, G.J.B., 1983. Implications of a sedimentary facies and depositional environmental  
1236 analysis of the Nama Group in South West Africa/Namibia. *Spec. Publ. Geol. Soc. South*  
1237 *Africa* 11, 89–114.
- 1238 Germs, G.J.B., Gresse, P.G., 1991. The foreland basin of the Damara and Gariep orogens in

1239 Namaqualand and southern Namibia: stratigraphic correlations and basin dynamics. *South*  
1240 *African J. Geol.* 94(2/3), 159-169.

1241 Geyman, E.C., Maloof, A.C., 2019. A diurnal carbon cycle engine explains  $^{13}\text{C}$ -enriched  
1242 carbonates without increasing the global production of oxygen. *Proc. Natl. Acad. Sci. U. S.*  
1243 *A.* 116, 24433–24439.

1244 Gozalo, R., Linán, E., Palacios, T., Gámez Vintaned, J.A., Mayoral, E., 2003. The Cambrian of  
1245 the Iberian Peninsula: An overview. *Geol. Acta* 1, 103–112.  
1246 <https://doi.org/10.1344/105.000001596>

1247 Gravestock, D.I., 1984. Archaeocyatha from lower parts of the Lower Cambrian carbonate  
1248 sequence in South Australia. *Mem. Assoc. Australas. Palaeontols.* 2, 1–139.

1249 Gravestock, D.I., Alexander, E.M., Demidenko, Y.E., Esakova, N. V., Holmer, L.E., Jago, J.B.,  
1250 Lin, T.-R., Melnikova, L.M., Parkhaev, P.Y., Rozanov, A.Y., Ushatinskaya, G.T., Zang,  
1251 W.-I., Zhegallo, E.A., Zhuravlev, A.Y., 2001. The Cambrian Biostratigraphy of the  
1252 Stansbury Basin, South Australia. Moscow: Nauka, 344p.

1253 Grazhdankin, D., 2014. Patterns of evolution of the Ediacaran Soft-Bodied Biota. *J. Paleontol.*  
1254 88, 269–283. <https://doi.org/10.1666/13-072>

1255 Grazhdankin, D., 2004. Patterns of distribution in the Ediacaran biotas: facies versus  
1256 biogeography and evolution. *Paleobiology* 30, 203–221. [https://doi.org/10.1666/0094-8373\(2004\)030<0203:podite>2.0.co;2](https://doi.org/10.1666/0094-8373(2004)030<0203:podite>2.0.co;2)

1257  
1258 Gresse, P.G., Germs, G.J.B., 1993. The Nama foreland basin: sedimentation, major unconformity  
1259 bounded sequences and multisided active margin advance. *Precambrian Res.* 63, 247-272.  
1260 [https://doi.org/10.1016/0301-9268\(93\)90036-2](https://doi.org/10.1016/0301-9268(93)90036-2)

1261 Grotzinger, J.P., Bowring, S.A., Saylor, B.Z., Kaufman, A.J., 1995. Biostratigraphic and  
1262 geochronological constraints on early animal evolution. *Science.* 13, 229–272.  
1263 <https://doi.org/10.1126/science.270.5236.598>

1264 Hahn, G., Pflug, H.D., 1985. Polypenartige Organismen aus dem Jung-Präkambrium (Nama-  
1265 Gruppe) von Namibia. *Geol. Palaeontol.* 19, 1–13.

1266 Halverson, G.P., Wade, B.P., Hurtgen, M.T., Barovich, K.M., 2010. Neoproterozoic  
1267 chemostratigraphy. *Precambrian Res.* 182, 337–350.  
1268 <https://doi.org/10.1016/j.precamres.2010.04.007>

1269 Hay, C.C., Creveling, J.R., Hagen, C.J., Maloof, A.C., Huybers, P., 2019. A library of early  
1270 Cambrian chemostratigraphic correlations from a reproducible algorithm. *Geology* 47, 457–  
1271 460.

1272 He, T., Zhu, M., Mills, B.J.W., Wynn, P.M., Zhuravlev, A.Y., Tostevin, R., Pogge von  
1273 Strandmann, P.A.E., Yang, A., Poulton, S.W., Shields, G.A., 2019. Possible links between  
1274 extreme oxygen perturbations and the Cambrian radiation of animals. *Nat. Geosci.* 12, 468–  
1275 474. <https://doi.org/10.1038/s41561-019-0357-z>

1276 Hodgkin, E.B., Nelson, L.L., Wall, C.J., Barrón-Díaz, A.J., Webb, L.C., Schmitz, M.D., Fike,  
1277 D.A., Hagadorn, J.W., Smith, E.F., 2020. A link between rift-related volcanism and end-  
1278 Ediacaran extinction? Integrated chemostratigraphy, biostratigraphy, and U-Pb  
1279 geochronology from Sonora, Mexico. *Geology* 49, 115–119.

1280 Hoffman, P.F., Lamothe, K.G., 2019. Seawater-buffered diagenesis, destruction of carbon  
1281 isotope excursions, and the composition of DIC in Neoproterozoic oceans. *Proc. Natl. Acad.*  
1282 *Sci. U. S. A.* 116, 18874–18879.

1283 Huang, T., Chen, D., Ding, Y., Zhou, X., Zhang, G., 2020. SIMS U-Pb zircon geochronological  
1284 and carbon isotope chemostratigraphic constraints on the Ediacaran-Cambrian boundary

1285           succession in the Three Gorges Area, South China. *J. Earth Sci.* 31, 69–78.

1286 Ishikawa, T., Ueno, Y., Komiya, T., Sawaki, Y., Han, J., Shu, D., Li, Y., Maruyama, S.,  
1287 Yoshida, N., 2008. Carbon isotope chemostratigraphy of a Precambrian/Cambrian boundary  
1288 section in the Three Gorge area, South China: Prominent global-scale isotope excursions  
1289 just before the Cambrian Explosion. *Gondwana Res.* 14, 193–208.  
1290 <https://doi.org/10.1016/j.gr.2007.10.008>

1291 Jablonski, D., Roy, K., Valentine, J.W., 2006. Out of the Tropics: Evolutionary Dynamics of the  
1292 Latitudinal Diversity Gradient. *Science.* 314, 102–106.

1293 Jago, J.B., Gehling, J.G., Betts, M.J., Brock, G.A., Dalgarno, C.R., García-Bellido, D.C., Haslett,  
1294 P.G., Jacquet, S.M., Kruse, P.D., Langsford, N.R., Mount, T.J., 2020. The Cambrian System  
1295 in the Arrowie Basin, Flinders Ranges, South Australia. *Aust. J. Earth Sci.* 67, 923–948.

1296 Jensen, S., Saylor, B.Z., Gehling, J.G., Germs, G.J.B., 2000. Complex trace fossils from the  
1297 terminal Proterozoic of Namibia. *Geology* 28, 143–146.

1298 Jiang, G., Kaufman, A.J., Christie-Blick, N., Zhang, S., Wu, H., 2007. Carbon isotope variability  
1299 across the Ediacaran Yangtze platform in South China: Implications for a large surface-to-  
1300 deep ocean  $\delta^{13}\text{C}$  gradient. *Earth Planet. Sci. Lett.* 261, 303–320.  
1301 <https://doi.org/10.1016/j.epsl.2007.07.009>

1302 Kaufman, A.J., Hayes, J.M., Knoll, A.H., Germs, G.J.B., 1991. Isotopic compositions of  
1303 carbonates and organic carbon from upper Proterozoic successions in Namibia: stratigraphic  
1304 variation and the effects of diagenesis and metamorphism. *Precambrian Res.* 49, 301–327.  
1305 [https://doi.org/10.1016/0301-9268\(91\)90039-D](https://doi.org/10.1016/0301-9268(91)90039-D)

1306 Kaufman, A.J., Jacobsen, S.B., Knoll, A.H., 1993. The Vendian record of Sr and C isotopic  
1307 variations in seawater: Implications for tectonics and paleoclimate. *Earth Planet. Sci. Lett.*  
1308 120, 409–430.

1309 Keith, M.L., Weber, J.N., 1964. Carbon and oxygen isotopic compositions of selected limestones  
1310 and fossils. *Geochim. Cosmochim. Acta* 28, 1787–1816.

1311 Knoll, A.H., Grotzinger, J.P., Kaufman, A.J., Kolosov, P.N., 1995. Integrated approaches to  
1312 terminal Proterozoic stratigraphy: An example from the Olenek Uplift, northeastern Siberia.  
1313 *Precambrian Res.* 73, 251–270.

1314 Korobov, M.N., 1989. Lower Cambrian biostratigraphy and polymeran trilobites of Mongolia.  
1315 *Sovmest. Sov.-Mongol. Geol. Ekspeditsiya, Trans.* 48, 1–204.

1316 Korobov, M.N., 1980. Lower Cambrian biostratigraphy and miomeran trilobites of Mongolia, in:  
1317 Menner, V. V., Meyen, S. V. (Eds.), *Lower Cambrian and Carboniferous Biostratigraphy of*  
1318 *Mongolia. Sovmest. Sov.-Mongol. Geol. Ekspeditsiya, Trans.* 26, pp. 5–108.

1319 Kouchinsky, A., Bengtson, S., Landing, E., Steiner, M., Vendrasco, M., Ziegler, K., 2017.  
1320 Terreneuvian stratigraphy and faunas from the Anabar Uplift, Siberia. *Acta Palaeontol. Pol.*  
1321 62. <https://doi.org/10.4202/app.00289.2016>

1322 Kouchinsky, A., Bengtson, S., Pavlov, V., Runnegar, B., Torssander, P., Young, E., Ziegler, K.,  
1323 2007. Carbon isotope stratigraphy of the Precambrian-Cambrian Sukharikha River section,  
1324 northwestern Siberian platform. *Geol. Mag.* 114, 1–10.  
1325 <https://doi.org/10.1017/S0016756807003354>

1326 Kouchinsky, A., Bengtson, S., Pavlov, V., Runnegar, B., Val'kov, A., Young, E., 2005. Pre-  
1327 Tommotian age of the lower Pestrotsvet Formation in the Selinde section on the Siberian  
1328 platform: carbon isotopic evidence. *Geol. Mag.* 142, 319–325.

1329 Kruse, P.D., Zhuravlev, A.Y., Parkhaev, P.Y., Zhu, M., 2017. A new lower Cambrian shelly  
1330 fossil biostratigraphy for South Australia, *Comment. Gondwana Res.* 44, 258–261.

- 1331 Landing, E., Kruse, P.D., 2017. Integrated stratigraphic, geochemical, and paleontological late  
1332 Ediacaran to early Cambrian records from southwestern Mongolia: Comment. Geol. Soc.  
1333 Am. Bull. 129, 7–8.
- 1334 Landing, E., Schmitz, M.D., Geyer, G., Trayler, R.B., Bowring, S.A., 2020. Precise early  
1335 Cambrian U-Pb zircon dates bracket the oldest trilobites and archaeocyaths in Moroccan  
1336 West Gondwana. Geol. Mag. 158, 219–238.
- 1337 Laurie, J.R., 1986. Phosphatic fauna of the Early Cambrian Todd River Dolomite, Amadeus  
1338 Basin, central Australia. Alcheringa 10, 431–454.
- 1339 Li, D., Ling, H.F., Shields-Zhou, G.A., Chen, X., Cremonese, L., Och, L., Thirlwall, M.,  
1340 Manning, C.J., 2013. Carbon and strontium isotope evolution of seawater across the  
1341 Ediacaran-Cambrian transition: Evidence from the Xiaotan section, NE Yunnan, South  
1342 China. Precambrian Res. 225, 128–147. <https://doi.org/10.1016/j.precamres.2012.01.002>
- 1343 Li, G.X., Zhao, X., Gubanov, A., Zhu, M.Y., Na, L., 2011. Early Cambrian mollusc *Watsonella*  
1344 *crobyi*: a potential GSSP index fossil for the base of Cambrian Stage 2. Acta Geol. Sin. 85,  
1345 309–319.
- 1346 Linnemann, U., Ovtcharova, M., Schaltegger, U., Gärtner, A., Hautmann, M., Geyer, G.,  
1347 Vickers-Rich, P., Rich, T., Plessen, B., Hofmann, M., Zieger, J., Krause, R., Kriesfeld, L.,  
1348 Smith, J., 2019. New high-resolution age data from the Ediacran-Cambrian boundary  
1349 indicate rapid, ecologically driven onset of the Cambrian explosion. Terra Nov. 31, 49–58.  
1350 <https://doi.org/10.1111/ter.12368>
- 1351 Lu, M., Zhu, M., Zhang, J., Shields-Zhou, G., Li, G., Zhao, F., Zhao, X., Zhao, M., 2013. The  
1352 DOUNCE event at the top of the Ediacaran Doushantuo Formation, South China: Broad  
1353 stratigraphic occurrence and non-diagenetic origin. Precambrian Res. 225, 86–109.  
1354 <https://doi.org/10.1016/j.precamres.2011.10.018>
- 1355 Macdonald, F.A., Strauss, J. V., Sperling, E.A., Halverson, G.P., Narbonne, G.M., Johnston,  
1356 D.T., Kunmann, M., Schrag, D.P., Higgins, J.A., 2013. The stratigraphic relationship  
1357 between the Shuram carbon isotope excursion, the oxygenation of Neoproterozoic oceans,  
1358 and the first appearance of the Ediacara biota and bilaterian trace fossils in northwestern  
1359 Canada. Chem. Geol. 362, 250–272.
- 1360 Maloney, K.M., Boag, T.H., Faccioli, A.J., Gibson, B.M., Cribb, A., Koester, B.E., Kenchington,  
1361 C.G., Racicot, R.A., Darroch, S.A.F., Laflamme, M., 2020. Palaeoenvironmental analysis of  
1362 *Ernietta*-bearing Ediacaran deposits in southern Namibia. Palaeogeogr. Palaeoclimatol.  
1363 Palaeoecol. 556, 109884.
- 1364 Maloof, A.C., Porter, S.M., Moore, J.L., Dudás, F.Ö., Bowring, S.A., Higgins, J.A., Fike, D.A.,  
1365 Eddy, M.P., 2010. The earliest Cambrian record of animals and ocean geochemical change.  
1366 Geol. Soc. Am. Bull. 122, 1731–1774. <https://doi.org/10.1130/B30346.1>
- 1367 Maloof, A.C., Schrag, D.P., Crowley, J.L., Bowring, S.A., 2005. An expanded record of Early  
1368 Cambrian carbon cycling from the Anti-Atlas Margin, Morocco. Can. J. Earth Sci. 42,  
1369 2195–2216. <https://doi.org/10.1139/e05-062>
- 1370 Matthews, J.J., Liu, A.G., Yang, C., McIlroy, D., Levell, B., Condon, D.J., 2020. A  
1371 chronostratigraphic framework for the rise of the Ediacaran microbiota: New constraints  
1372 from Mistaken Point Ecological Reserve, Newfoundland. Geol. Soc. Am. Bull. 133, 612–  
1373 624.
- 1374 Melim, L.A., Westphal, H., Swart, P.K., Eberli, G.P., Munnecke, A., 2002. Questioning  
1375 carbonate diagenetic paradigms: Evidence from the Neogene of the Bahamas. Mar. Geol.  
1376 185, 27–53.



1377 Merdith, A.S., Williams, S.E., Collins, A.S., Tetley, M.G., Mulder, J.A., Blades, M.L., Young,  
1378 A., Armistead, S., Cannon, J., Zahirovic, S., Müller, R.D., 2021. Extending full-plate  
1379 tectonic models into deep time: Linking the Neoproterozoic and Phanerozoic. *Earth-Science*  
1380 *Rev.* 214, 103477.

1381 Muscente, A.D., Bykova, N., Boag, T.H., Buatois, L.A., Mángano, M.G., Eleish, A., Prabhu, A.,  
1382 Pan, F., Meyer, M.B., Schiffbauer, J.D., Fox, P., Hazen, R.M., Knoll, A.H., 2019. Ediacaran  
1383 biozones identified with network analysis provide evidence for pulsed extinctions of early  
1384 complex life. *Nat. Commun.* 10, 1–15. <https://doi.org/10.1038/s41467-019-08837-3>

1385 Narbonne, G.M., Kaufman, A.J., Knoll, A.H., 1994. Integrated chemostratigraphy and  
1386 biostratigraphy of the Windermere Supergroup, northwestern Canada: Implications for  
1387 Neoproterozoic correlations and the early evolution of animals. *Geol. Soc. Am. Bull.* 106,  
1388 1281–1292.

1389 Narbonne, G.M., Saylor, B.Z., Grotzinger, J.P., 1997. The youngest Ediacaran fossils from  
1390 Southern Africa. *J. Paleontol.* 71, 953–967. <https://doi.org/10.1017/S0022336000035940>

1391 Noble, S.R., Condon, D.J., Carney, J.N., Wilby, P.R., Pharaoh, T.C., Ford, T.D., 2015. U-Pb  
1392 geochronology and global context of the Charnian Supergroup, UK: Constraints on the age  
1393 of key Ediacaran fossil assemblages. *Geol. Soc. Am. Bull.* 127, 250–265.

1394 Osadchaya, D. V., Kotel'nikov, D. V., 1998. Archaeocyathids from the Atdabanian (Lower  
1395 Cambrian) of the Altay-Sayan Foldbelt, Russia. *Geodiversitas* 20, 5–18.

1396 Parkhaev, P.Y., 2019. Cambrian mollusks of Australia: Taxonomy, biostratigraphy, and  
1397 Paleobiogeography. *Stratigr. Geol. Correl.* 27, 181–206.

1398 Parkhaev, P.Y., Karlova, G.A., 2011. Taxonomic revision and evolution of Cambrian molluscs  
1399 of the genus *Aldanella* Vostokova, 1962 (Gastropoda: Archaeobranchia). *Paleontol. J.* 45,  
1400 1145–1205.

1401 Parry, L.A., Boggiani, P.C., Condon, D.J., Garwood, R.J., Leme, J. de M., McIlroy, D., Brasier,  
1402 M.D., Trindade, R., Capanha, G.A.C., Pacheco, M.L.A.F., Diniz, C.Q.C., Liu, A., 2017.  
1403 Ichnological evidence for meiofaunal bilaterians from the terminal Ediacaran and earliest  
1404 Cambrian of Brazil. *Nat. Ecol. Evol.* 1, 1455–1464.

1405 Paterson, J.R., Edgecombe, G.D., Lee, M.S., 2019. Trilobite evolutionary rates constrain the  
1406 duration of the Cambrian explosion. *Proc. Natl. Acad. Sci. U. S. A.* 116, 4394–4399.

1407 Pelechaty, S.M., 1998. Integrated chronostratigraphy of the Vendian System of Siberia:  
1408 implications for a global stratigraphy. *Geol. Soc. London* 155, 957–973.

1409 Pelechaty, S.M., Grotzinger, J.P., Kashirtsev, V.A., Zhernovsky, V.P., 1996a.  
1410 Chemostratigraphic and sequence stratigraphic constraints on Vendian-Cambrian basin  
1411 dynamics, Northeast Siberian Craton. *J. Geol.* 104, 543–563.

1412 Pelechaty, S.M., Kaufman, A.J., Grotzinger, J.P., 1996b. Evaluation of  $\delta^{13}\text{C}$  chemostratigraphy  
1413 for intrabasinal correlation: Vendian strata of northeast Siberia. *Bull. Geol. Soc. Am.* 108,  
1414 992–1003. [https://doi.org/10.1130/0016-7606\(1996\)108<0992:EOCCFI>2.3.CO;2](https://doi.org/10.1130/0016-7606(1996)108<0992:EOCCFI>2.3.CO;2)

1415 Pickford, M.H.L., 1995. Review of the Riphean, Vendian and early Cambrian palaeontology of  
1416 the Otavi and Nama groups, Namibia. *Commun. - Geol. Surv. Namibia* 10, 57–81.

1417 Porter, S.M., 2007. Seawater chemistry and early carbonate biomineralization. *Science.* 316,  
1418 1302.

1419 Prave, A.R., Kirsimäe, K., Lepland, A., Fallick, A.E., Kreitsmann, T., Deines, Y.E., Romashkin,  
1420 A.E., Rychanchik, D.V., Medvedev, P.V., Moussavou, M., Bakakas, K., 2021. The grandest  
1421 of them all: the Lomagundi-Jatuli Event and Earth's oxygenation. *J. Geol. Soc. London.*

1422 Rogov, V.I., Karlova, G.A., Marusin, V. V., Kochnev, B.B., Nagovitsin, K.E., Grazhdankin, D.

- 1423 V., 2015. Duration of the first biozone in the Siberian hypostratotype of the Vendian. *Russ.*  
1424 *Geol. Geophys.* 56, 573–583.
- 1425 Rooney, A.D., Cantine, M.D., Bergmann, K.D., Gómez-Pérez, I., Al Baloushi, B., Boag, T.H.,  
1426 Busch, J.F., Sperling, E.A., Strauss, J. V., 2020. Calibrating the coevolution of Ediacaran  
1427 life and environment. *Proc. Natl. Acad. Sci. U. S. A.* 117, 16824–16830.
- 1428 Saylor, B.Z., 2003. Sequence stratigraphy and carbonate-siliciclastic mixing in a terminal  
1429 Proterozoic foreland basin, Urusis Formation, Nama Group, Namibia. *J. Sediment. Res.* 73,  
1430 264–279. <https://doi.org/10.1306/082602730264>
- 1431 Saylor, Beverly Z., Grotzinger, J.P., 1996. Reconstruction of important Proterozoic-Cambrian  
1432 boundary exposures through the recognition of thrust deformation in the Nama Group of  
1433 southern Namibia. *Communs geol. Surv. Namibia* 11, 1–12.
- 1434 Saylor, B.Z., Grotzinger, J.P., Germs, G.J.B., 1995. Sequence stratigraphy and sedimentology of  
1435 the Neoproterozoic Kuibis and Schwarzrand Subgroups (Nama Group), southwestern  
1436 Namibia. *Precambrian Res.* 73, 153–171. [https://doi.org/10.1016/0301-9268\(94\)00076-4](https://doi.org/10.1016/0301-9268(94)00076-4)
- 1437 Saylor, B.Z., Kaufman, A.J., Grotzinger, J.P., Urban, F., 1998. A composite reference section for  
1438 terminal Proterozoic strata of southern Namibia. *J. Sediment. Res.* 68, 1223–1235.  
1439 <https://doi.org/10.2110/jsr.68.1223>
- 1440 Schmitz, M.D., 2012. Radiogenic Isotope Geochronology, in: Gradstein, F.M., Ogg, J.G.,  
1441 Schmitz, M.D., Ogg, G.M. (Eds.), *The Geological Time Scale 2012*. Elsevier, pp. 115–126.
- 1442 Smith, E.F., Macdonald, F.A., Petach, T.A., Bold, U., Schrag, D.P., 2015. Integrated  
1443 stratigraphic, geochemical, and paleontological late Ediacaran to early Cambrian records  
1444 from southwestern Mongolia. *Geol. Soc. Am. Bull.* 128, 442–468.  
1445 <https://doi.org/10.1130/B31248.1>
- 1446 Smith, E.F., Nelson, L.L., Strange, M.A., Eyster, A.E., Rowland, S.M., Schrag, D.P.,  
1447 Macdonald, F.A., 2016. The end of the Ediacaran: Two new exceptionally preserved body  
1448 fossil assemblages from Mount Dunfee, Nevada, USA. *Geology* 44, 911–914.  
1449 <https://doi.org/10.1130/G38157.1>
- 1450 Smith, O., 1998. Terminal Proterozoic Carbonate Platform Development: Stratigraphy and  
1451 Sedimentology of the Kuibis Subgroup (ca. 550 – 548 Ma), Northern Nama Basin,  
1452 Namibia. Massachusetts Institute of Technology.
- 1453 Steiner, M., Yang, B., Hohl, S., Zhang, L., Chang, S., 2020. Cambrian small skeletal fossil and  
1454 carbon isotope records of the southern Huangling Anticline, Hubei (China) and implications  
1455 for chemostratigraphy of the Yangtze Platform. *Palaeogeogr. Palaeoclimatol. Palaeoecol.*  
1456 554, 109817.
- 1457 Tahata, M., Ueno, Y., Ishikawa, T., Sawaki, Y., Murakami, K., Han, J., Shu, D., Li, Y., Guo, J.,  
1458 Yoshida, N., Komiya, T., 2013. Carbon and oxygen isotope chemostratigraphies of the  
1459 Yangtze platform, South China: Decoding temperature and environmental changes through  
1460 the Ediacaran. *Gondwana Res.* 23, 333–353. <https://doi.org/10.1016/j.gr.2012.04.005>
- 1461 Uhlein, G.J., Uhlein, A., Periera, E., Caxito, F.A., Okubo, J., Warren, L. V., Sial, A.N., 2019.  
1462 Ediacaran paleoenvironmental changes recorded in the mixed carbonate-siliciclastic  
1463 Bambuí Basin, Brazil. *Palaeogeogr. Palaeoclimatol. Palaeoecol.* 517, 39–51.
- 1464 Veizer, J., Hoefs, J., 1976. The nature of  $^{18}\text{O}/^{16}\text{O}$  and  $^{13}\text{C}/^{12}\text{C}$  secular trends in sedimentary  
1465 carbonate rocks. *Geochim. Cosmochim. Acta* 40, 1387–1395.
- 1466 Veizer, J., Holser, W.T., Wilgus, C.K., 1980. Correlation of  $^{13}\text{C}/^{12}\text{C}$  and  $^{34}\text{S}/^{32}\text{S}$  secular  
1467 variations. *Geochim. Cosmochim. Acta* 44, 579–587.
- 1468 Vernhet, E., 2007. Paleobathymetric influence on the development of the late Ediacaran Yangtze

1469 platform (Hubei, Hunan, and Guizhou provinces, China). *Sediment. Geol.* 197, 29–46.

1470 Vishnevskaya, I.A., Kochnev, B.B., Letnikova, E.F., Kiseleva, V.Y., Pisareva, N.I., 2013. Sr  
1471 isotope signatures in the Vendian Khorbusuonka Group of the Olenek Uplift (northeastern  
1472 Siberian Platform). *Dokl. Earth Sci.* 449, 298–302.

1473 Vishnevskaya, I.A., Letnikova, E.F., Vetrova, N.I., Kochnev, B.B., Dil, S.I., 2017.  
1474 Chemostratigraphy and detrital zircon geochronology of the Neoproterozoic Khorbusuonka  
1475 Group, Olenek Uplift, Northeastern Siberian platform. *Gondwana Res.* 51, 255–271.

1476 Wang, W., Guan, C., Zhou, C., Peng, Y., Pratt, L.M., Chen, X., Chen, L., Chen, Z., Yuan, X.,  
1477 Xiao, S., 2017. Integrated carbon, sulfur, and nitrogen isotope chemostratigraphy of the  
1478 Ediacaran Lantian Formation in South China: Spatial gradient, ocean redox oscillation, and  
1479 fossil distribution. *Geobiology* 15, 552–571. <https://doi.org/10.1111/gbi.12226>

1480 Wang, W., Zhou, C., Guan, C., Yuan, X., Chen, Z., Wan, B., 2014. An integrated carbon,  
1481 oxygen, and strontium isotopic studies of the Lantian Formation in South China with  
1482 implications for the Shuram anomaly. *Chem. Geol.* 373, 10–26.  
1483 <https://doi.org/10.1016/j.chemgeo.2014.02.023>

1484 Warren, L.V., Buatois, L., Mangano, M.G., Simões, M.G., Santos, M.G.M., Poiré, D.,  
1485 Riccomini, C., Assine, M.L., 2020. Microbially induced pseudotraces from a Pantanal soda  
1486 lake, Brazil: Alternative interpretations for Ediacaran simple trails and their limits. *Geology*  
1487 48, G472341.

1488 Warren, L. V., Fairchild, T.R., Gaucher, C., Boggiani, P.C., Poiré, D.G., Anelli, L.E., Inchausti,  
1489 J.C.G., 2011. *Corumbella* and in situ *Cloudina* in association with thrombolites in the  
1490 Ediacaran Itapucumi Group, Paraguay. *Terra Nov.* 23, 382–389.  
1491 <https://doi.org/10.1111/j.1365-3121.2011.01023.x>

1492 Wood, R.A., Liu, A.G., Bowyer, F.T., Wilby, P.R., Dunn, F.S., Kenchington, C.G., Hoyal  
1493 Cuthill, J.F., Mitchell, E.G., Penny, A.M., 2019. Integrated records of environmental change  
1494 and evolution challenge the Cambrian Explosion. *Nat. Ecol. Evol.* 3, 528–538.

1495 Wood, R.A., Poulton, S.W., Prave, A.R., Hoffmann, K.-H., Clarkson, M.O., Guilbaud, R., Lyne,  
1496 J.W., Tostevin, R., Bowyer, F., Penny, A.M., Curtis, A., Kasemann, S.A., 2015. Dynamic  
1497 redox conditions control late Ediacaran metazoan ecosystems in the Nama Group, Namibia.  
1498 *Precambrian Res.* 261, 252–271. <https://doi.org/10.1016/j.precamres.2015.02.004>

1499 Xiao, S., Chen, Z., Pang, K., Zhou, C., Yuan, X., 2020. The Shibantan Lagerstätte: insights into  
1500 the Proterozoic-Phanerozoic transition. *J. Geol. Soc. London.* 178.

1501 Xiao, S.H., Narbonne, G.M., 2020. The Ediacaran Period, in: Gradstein, F.M., Ogg, J.G.,  
1502 Schmitz, M.D., Ogg, G.M. (Eds.), *Geological Time Scale 2020*. Elsevier B.V., pp. 521–561.

1503 Yang, A., Zhu, M., Zhuravlev, A.Y., Yuan, K., Zhang, J., Chen, Y., 2016. Archaeocyathan  
1504 zonation of the Yangtze Platform: implications for regional and global correlation of lower  
1505 Cambrian stages. *Geol. Mag.* 153, 388–409.

1506 Yang, B., Steiner, M., Zhu, M., Li, G., Liu, J., Liu, P., 2016. Transitional Ediacaran–Cambrian  
1507 small skeletal fossil assemblages from South China and Kazakhstan: Implications for  
1508 chronostratigraphy and metazoan evolution. *Precambrian Res.* 285, 202–215.

1509 Yang, C., Rooney, A.D., Condon, D.J., Li, X.-H., Grazhdankin, D. V., Bowyer, F.T., Hu, C.,  
1510 Macdonald, F., Zhu, M., 2021. The tempo of Ediacaran evolution. *Sci. Adv.* 7, eabi9643.

1511 Zhou, C., Xiao, S., Wang, W., Guan, C., Ouyang, Q., Chen, Z., 2017. The stratigraphic  
1512 complexity of the middle Ediacaran carbon isotopic record in the Yangtze Gorges area,  
1513 South China, and its implications for the age and chemostratigraphic significance of the  
1514 Shuram excursion. *Precambrian Res.* 288, 23–38.

1515 <https://doi.org/10.1016/j.precamres.2016.11.007>  
1516 Zhu, M., Lu, M., Zhang, J., Zhao, F., Li, G., Aihua, Y., Zhao, X., Zhao, M., 2013. Carbon  
1517 isotope chemostratigraphy and sedimentary facies evolution of the Ediacaran Doushantuo  
1518 Formation in western Hubei, South China. *Precambrian Res.* 225, 7–28.  
1519 <https://doi.org/10.1016/j.precamres.2011.07.019>  
1520 Zhu, M., Zhang, J., Yang, A., 2007. Integrated Ediacaran (Sinian) chronostratigraphy of South  
1521 China. *Palaeogeogr. Palaeoclimatol. Palaeoecol.* 254, 7–61.  
1522 <https://doi.org/10.1016/j.palaeo.2007.03.025>  
1523 Zhu, M., Zhuravlev, A.Y., Wood, R.A., Zhao, F., Sukhov, S.S., 2017. A deep root for the  
1524 Cambrian explosion: Implications of new bio- and chemostratigraphy from the Siberian  
1525 Platform. *Geology* 45, 459–462.  
1526 Zhuravlev, A.Y., 1998. Early Cambrian archaeocyathan assemblages of Mongolia. *Lund Publ.*  
1527 *Geol.* 142, 24–25.  
1528 Zhuravlev, A.Y., Gravestock, D.I., 1994. Archaeocyaths from Yorke Peninsula, South Australia  
1529 and archaeocyathan Early Cambrian zonation. *Alcheringa* 18, 1–54.  
1530 Zhuravlev, A.Y., Naimark, E.B., 2005. Alpha, beta, or gamma: Numerical view on the Early  
1531 Cambrian world. *Palaeogeogr. Palaeoclimatol. Palaeoecol.* 220, 207–225.  
1532 Zhuravleva, I.T., Konyaeva, I.A., Osadchaya, D. V., Boyarinov, A.S., 1997. Biostratigraphy of  
1533 the Kiya River section. Early Cambrian archaeocyaths and spicular sponges from the Kiya  
1534 River section (Kuznetsk Alatau). *Ann. Paleontol.* 83, 115–200.  
1535  
1536